



UPPSALA
UNIVERSITET

*Digital Comprehensive Summaries of Uppsala Dissertations
from the Faculty of Science and Technology 900*

Modelling Band Gap Gradients and Cd-free Buffer Layers in Cu(In,Ga)Se₂ Solar Cells

JONAS PETTERSSON



ACTA
UNIVERSITATIS
UPSALIENSIS
UPPSALA
2012

ISSN 1651-6214
ISBN 978-91-554-8280-0
urn:nbn:se:uu:diva-168618

Dissertation presented at Uppsala University to be publicly examined in Polhemssalen, Ångströmlaboratoriet, Lägerhyddsvägen 1, Uppsala. Friday, March 30, 2012 at 13:15 for the degree of Doctor of Philosophy. The examination will be conducted in English.

Abstract

Pettersson, J. 2012. Modelling Band Gap Gradients and Cd-free Buffer Layers in Cu(In,Ga)Se₂ Solar Cells. Acta Universitatis Upsaliensis. *Digital Comprehensive Summaries of Uppsala Dissertations from the Faculty of Science and Technology* 900. 70 pp. Uppsala. ISBN 978-91-554-8280-0.

A deeper understanding of Cu(In,Ga)Se₂ (CIGS) solar cells is important for the further improvement of these devices. This thesis is focused on the use of electrical modelling as a tool for pursuing this aim. Finished devices and individual layers are characterized and the acquired data are used as input in the simulations. Band gap gradients are accounted for when modelling the devices. The thesis is divided into two main parts. One part that treats the influence of cadmium free buffer layers, mainly atomic layer deposited (Zn,Mg)O, on devices and another part in which the result of CIGS absorber layer modifications is studied. Recombination analysis indicates that interface recombination is limiting the open circuit voltage (V_{oc}) in cells with ZnO buffer layers. This recombination path becomes less important when magnesium is introduced into the ZnO giving a positive conduction band offset (CBO) towards the CIGS absorber layer. Light induced persistent photoconductivity (PPC) is demonstrated in (Zn,Mg)O thin films. Device modelling shows that the measured PPC, coupled with a high density of acceptors in the buffer-absorber interface region, can explain light induced metastable efficiency improvement in CIGS solar cells with (Zn,Mg)O buffer layers. It is shown that a thin indium rich layer closest to the buffer does not give any significant impact on the performance of devices dominated by recombination in the CIGS layer. In our cells with CdS buffer the diffusion length in the CIGS layer is the main limiting factor. A thinner CIGS layer improves V_{oc} by reducing recombination. However, for thin enough absorber layers V_{oc} deteriorates due to recombination at the back contact. Interface recombination is a problem in thin devices with Zn(O,S) buffer layers. This recombination path is overshadowed in cells of standard thickness by recombination in the CIGS bulk. Thin cells with Zn(O,S) buffer layers have a higher efficiency than CdS cells with the same absorber thickness.

Keywords: CIGS, Thin film solar cells, Electrical modelling, Alternative buffer layers, Gallium gradients, Simulations, Electrical characterization, Metastabilities, Light-soaking, Hall measurements, Persistent photoconductivity

Jonas Pettersson, Uppsala University, Department of Engineering Sciences, Solid State Electronics, Box 534, SE-751 21 Uppsala, Sweden.

© Jonas Pettersson 2012

ISSN 1651-6214

ISBN 978-91-554-8280-0

urn:nbn:se:uu:diva-168618 (<http://urn.kb.se/resolve?urn=urn:nbn:se:uu:diva-168618>)

*Solen glider fram bakom husväggen
ställer sig mitt i gatan
och andas på oss
med sin röda blåst.*

Tomas Tranströmer, *Landskap med solar*
Sorgegondolen (1996)

List of Papers

This thesis is based on the following papers, which are referred to in the text by their Roman numerals.

- I A. Hultqvist , C. Platzer-Björkman, J. Pettersson, T. Törndahl and M. Edoff, CuGaSe₂ solar cells using atomic layer deposited Zn(O,S) and (Zn,Mg)O buffer layers Thin Solid Films 517 (2009) pp. 2305-2308, doi:10.1016/j.tsf.2008.10.109
- II J. Pettersson, C. Platzer-Björkman and M. Edoff, Temperature-dependent current-voltage and lightsoaking measurements on Cu(In,Ga)Se₂ solar cells with ALD-Zn_{1-x}Mg_xO buffer layers, Progress in Photovoltaics: Research and Applications 17 (2009) pp. 460-469, doi:10.1002/pip.912
- III J. Pettersson, C. Platzer-Björkman, A. Hultqvist , U. Zimmerman and M. Edoff, Measurements of photo-induced changes in the conduction properties of ALD-Zn_{1-x}Mg_xO thin films, Physica Scripta T141 (2010) 014010, doi:10.1088/0031-8949/2010/T141/014010
- IV J. Pettersson, C. Platzer-Björkman, U. Zimmerman and M. Edoff, Baseline model of graded-absorber Cu(In,Ga)Se₂ solar cells applied to cells with Zn_{1-x}Mg_xO buffer layers, Thin Solid Films 519 (2011) pp. 7476-7480, doi:10.1016/j.tsf.2010.12.141
- V S. Schleussner, J. Pettersson, T. Törndahl and M. Edoff, Surface engineering in Cu(In,Ga)Se₂ solar cells, Published online by Progress in Photovoltaics: Research and Applications, doi: 10.1002/pip.1229
- VI J. Pettersson, M. Edoff and C. Platzer-Björkman, Electrical modelling of Cu(In,Ga)Se₂ cells with ALD-Zn_{1-x}Mg_xO buffer layers, Journal of Applied Physics 111 (2012) 014509, doi: 10.1063/1.3672813
- VII J. Pettersson, T. Törndahl, C. Platzer-Björkman, A. Hultqvist, M. Edoff, Influence of absorber thickness on Cu(In,Ga)Se₂ solar cells with different buffer layers, Manuscript

Reprints were made with permission from the publishers.

Personal Contributions to the Papers

- I The article was written by Adam Hultqvist. I performed JVT measurements on the devices and analysed the results.
- II I performed the electrical measurements, analysed the results and wrote the article.
- III I developed the project, performed the electrical measurements and wrote the article.
- IV I wrote the article and developed the electrical models.
- V Sebastian Schleussner wrote most of the article. I helped him with the JVT and CVT measurements and analysis. Additionally, I developed the electrical models and wrote the parts of the article concerning simulations.
- VI I wrote the article, performed light soaking measurements, developed the device models and analysed the simulation results.
- VII I wrote most of the the article, performed electrical and optical characterization and developed the electrical models.

Related Papers, not Included in the Thesis

- i C. Platzer-Björkman, P. Zabierowski, J. Pettersson, T. Törndahl and M. Edoff, Improved fill factor and open circuit voltage by crystalline selenium at the Cu(In,Ga)Se₂/buffer layer interface in thin film solar cells, Progress in Photovoltaics: Research and Applications, v 18, n 4 (2010) pp. 249-256, doi:10.1002/pip.957
- ii C. Platzer-Björkman, A. Hultqvist, J. Pettersson and T. Törndahl, Band gap engineering of ZnO for high efficiency CIGS based solar cells, Proceedings of SPIE Vol. 7603 (2010) 76030F, doi:10.1117/12.846017

Contents

List of Papers	v
Related Papers, not Included in the Thesis	vii
1 Introduction	1
1.1 Photovoltaics	1
1.2 CIGS Thin-Film Solar Cells	3
1.3 Aim of Thesis	5
2 Characterization Methods	7
2.1 Current-Voltage Measurements	7
2.2 Quantum-Efficiency Measurements	12
2.3 Capacitance-Voltage Profiling	14
2.4 Resistivity and Hall Measurements	17
2.5 CIGS Compositional Analysis	18
2.6 Optical Characterization	19
3 Electrical Modelling and Simulations	21
3.1 Basic Equations	21
3.2 Modelling Software	22
3.3 Parameter Selection	23
4 Modelling and Measurement Results	29
4.1 Results of Simulations Using the Baseline Parameter Set	29
4.2 Electrical Characteristics of CIGS-Cells with Alternative Buffer Layers	35
4.3 Results of Absorber Layer Modifications	46
4.4 A Discussion on Metastabilities	52
5 Conclusions	55
Sammanfattning på svenska	56
Acknowledgements	60
Bibliography	63

Glossary

AC alternating current. 14, 15

ALD atomic layer deposition. 4, 12, 35, 38, 40, 41, 46

CBD chemical bath deposition. 46

CBO conduction band offset. 26, 27, 31, 33, 40, 41, 46, 48, 55

CGS CuGaSe_2 . 3, 12, 14, 23, 24, 46, 47

CIGS Cu(In,Ga)Se_2 . 1, 3–5, 7, 9, 11–16, 18, 20, 23, 24, 26, 27, 29, 31, 34, 35, 38, 40, 46–50, 52, 55, 56

CIS CuInSe_2 . 3, 23, 26, 47–49, 55

CV capacitance-voltage. 14–16, 22, 24, 47, 48

DC direct current. 14, 15

EQE external quantum efficiency. 12, 13, 27

FF fill factor. 7, 38, 40, 43, 53, 55

IPES inverse photo-electron spectroscopy. 26

IQE internal quantum efficiency. 13, 27, 50, 51

JV current-voltage. 7, 8, 10, 12, 22–24, 26, 27, 29, 30, 39, 40, 43, 45, 47, 48

JVT temperature-dependent JV. 10, 12, 15, 24, 26, 40, 47, 52, 55

LED light-emitting diode. 9, 35, 37, 43, 52

LS light-soaking. 9, 12, 35

MBE molecular beam epitaxy. 38

PPC persistent photo conductivity. 35, 37, 38, 43, 52, 55

QE quantum efficiency. 8, 13, 14, 22–24, 26, 27, 29, 30, 47–50, 52, 56

RT room temperature. 9, 29, 30, 35, 43

SDL surface defect layer. 23, 25, 26, 29–35, 41, 43, 46

SIMS secondary ion mass spectrometry. 18, 19, 24, 29, 47

SLG soda-lime glass. 3, 18

STC standard test condition. 8, 13

TEM transmission electron microscopy. 3, 4

UV ultra-violet. 9, 35–37, 40, 43, 52

VBO valence band offset. 26, 40, 43, 46

XPS x-ray photoelectron spectroscopy. 18, 19, 24

XRF x-ray fluorescence. 18, 19, 24, 29, 35, 50

XRR x-ray reflectivity. 35

1. Introduction

The demand of energy in the world is steadily increasing year by year. The current total final consumption of energy amounts to about 100 PWh [6]. Even if this is a huge number, it is small in comparison to the energy arriving on earth by solar irradiation. On a clear summer day the irradiation on earth's surface is about 1 kW m^{-2} . Each minute of solar irradiation on earth is enough for several days of human consumption. Direct solar energy is a vast and largely unused energy resource. One way to utilize this resource is by using photovoltaic devices.

1.1 Photovoltaics

Photovoltaic devices, in other words solar cells, are devices that convert light into electricity. There are several different solar cell techniques but the most established type is the solid state semiconductor solar cell. The light absorbing layer in these cells can either be a crystalline, polycrystalline or amorphous semiconductor. Silicon is the most widely used material for solar cells. Silicon solar cells are together with GaAs cells the most efficient single junction devices [21]. Other material, such as CdTe and Cu(In,Ga)Se_2 (CIGS) have grown in importance during recent years. These materials are mainly deposited as polycrystalline thin-films. One advantage of these materials in comparison to crystalline or polycrystalline silicon is the good light absorption properties which reduces the required layer thickness from about a hundred μm down to only a few μm . This makes them potentially cheaper to produce if an efficient fabrication method is applied.

Semiconductors have distinct bands of electron states, the so called valence and conduction bands. These are separated by a forbidden gap of energies, the band gap, where, for the ideal crystalline material, no electron states exists. At a temperature of 0 K states up to the valence band maximum are filled with electrons while the conduction band is empty. At higher temperatures some electrons are thermally excited across the band gap and leave behind holes in the valence band. The electron occupancy of the conduction band at a certain temperature is higher the lower the band gap of a material is. The electron and hole occupancies of the bands follow the Fermi-Dirac distribution. This distribution is characterized by the Fermi energy, at which the probability of occupation of a state is one half [70, 71].

Doping in a semiconductor is due to states in the band gap close to the band edges. These states can easily be ionized and thus contribute with additional free carriers to the bands. States close to the valence band and conduction band result in p-doping and n-doping, respectively. If a material is n-doped there are more free electrons than holes and the equilibrium Fermi level lies closer to the conduction band than the valence band, while a p-doped material has an excess of free holes and a Fermi level lying closer to the valence band. Doping can either be extrinsic, caused by a foreign atoms entering the host crystal, or intrinsic, caused by various other types of defects in the crystal structure.

A pn-diode consists of a p-type and an n-type semiconductor brought together. Due to diffusion of electrons from the n-side towards the p-side and holes from the p-side towards the n-side a depletion region virtually empty of free carriers emerges, surrounding the pn-junction. The ionized dopants in the depletion region sets up an electric field, the so called built-in-field, that causes a drift current set in the opposite direction to the diffusion current. These contributions to the current cancel each other in equilibrium.

The total current density as a function of voltage is given by the ideal diode law in Equation 1.1.

$$J = J_0 \left(e^{\frac{qV}{kT}} - 1 \right) - J_L \quad (1.1)$$

Here J_0 is the saturation current density, k is the Boltzmann constant while T is the temperature. The positive direction of current is taken from the p-side towards the n-side of the junction. In Figure 1.1 the band diagram of a pn-junction is sketched. In this example the band gap and doping density are the same on the p-side as on the n-side.

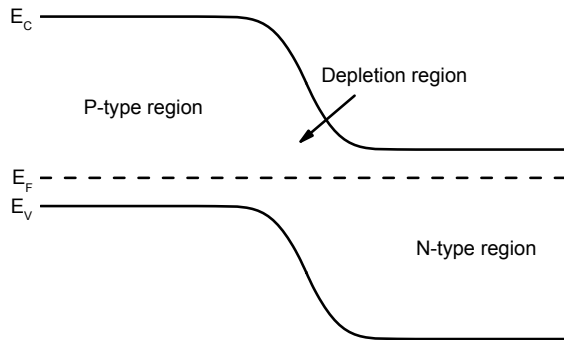


Figure 1.1: Band diagram of a pn-junction in equilibrium. The conduction band (E_C), valence band (E_V) and Fermi level (E_F) are shown.

A semiconductor solar cell is essentially a pn-diode fabricated from suitable light-absorbing materials. Under illumination, photons with energies higher than the band gap of the material are absorbed by electrons in the valence band. These electrons are excited to the conduction band and thereby excess electron-hole pairs are generated. These pairs may be separated by the built-in field if the carriers are generated either within the depletion region or close enough to be able to diffuse into it. The separated holes and electrons create a current from the n-doped side towards the p-doped side of the junction.

1.2 CIGS Thin-Film Solar Cells

1.2.1 Overview

CIGS is a direct band gap semiconductor with a chalcopyrite crystalline structure. Numerous techniques have been used to deposit CIGS layers for the use in solar cells. Some examples are co-evaporation, sputtering followed by selenization, chemical vapour deposition, spray pyrolysis and electro-chemical deposition. Of all methods the most successful, in terms of highest solar cell efficiency, is co-evaporation from elemental sources (see [29] and references therein).

The CIGS composition is often described using two concentration ratios $[\text{Cu}]/([\text{Ga}]+[\text{In}])$ and $[\text{Ga}]/([\text{Ga}]+[\text{In}])$. These parameters are abbreviated Cu/III and Ga/III or CGI and GGI. The band gap increases with Ga-content. Pure CuInSe_2 (CIS) has a band gap of 1.0 eV while pure CuGaSe_2 (CGS) has a band gap between 1.6 eV and 1.7 eV [67].

The record efficiency of a CIGS solar cell is 20.3 %, which was recently reached by Jackson et. al. for a lab-scale device [25].

1.2.2 Layer and Device Processing

A CIGS solar cell is built up of a number of layers of different materials. This can be seen in the transmission electron microscopy (TEM) cross-section of Figure 1.2 depicting a solar cell stack fabricated at the Ångström Solar Center.

In Ångström Solar Center we both fabricate small area test solar cells and mini-modules composed of several monolithically interconnected cells. In this thesis I focus on studying test cells with an area of 0.5 cm^2 each.

In our baseline fabrication process presented by Kessler et. al. [30] we use soda-lime glass (SLG) as substrate. On top of this we sputter a molybdenum back contact. For CIGS deposition we have three different co-evaporation chambers at our disposal. In Paper I we use both the UMS evaporation chamber that uses end-point detection to control the final Cu-content and the BAK chamber that uses a mass spectrometer to control the rates of the evaporation sources according to some pre-programmed profiles [7]. We also fabricated

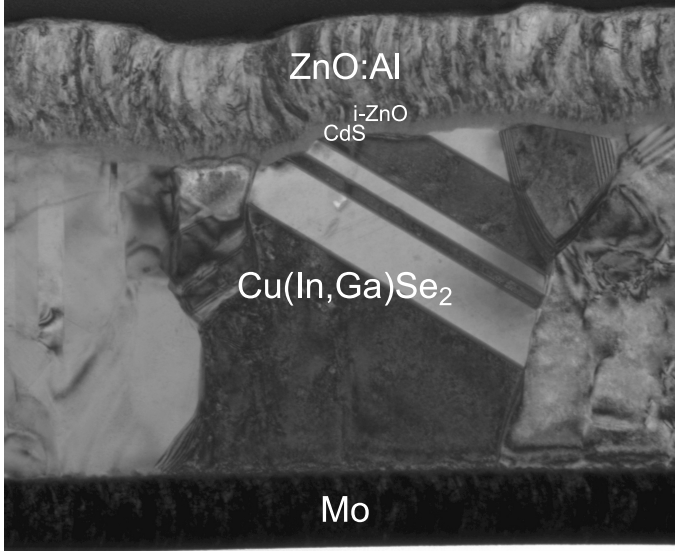


Figure 1.2: Cross-section image of CIGS device acquired by TEM. The constituent materials are indicated.

the cells of Paper V in the BAK chamber. Here we utilized the three-stage process that is commonly applied to deposit high-efficiency CIGS [18, 26, 59]. The devices of Papers II and VII were produced in an in-line evaporator denoted MrPilote [15]. The substrates move through this chamber passing immobile evaporation sources .

CdS, deposited in a chemical bath, is used as a so called buffer layer on top of the CIGS absorber, in our baseline recipe. The disadvantages with CdS is the relatively low band gap of 2.4eV. This results in a loss of efficiency since few of the charge-carriers generated in the buffer layer are collected at the contacts. Furthermore, cadmium is toxic and the use in electronics is therefore restricted in the European Union [1]. The study of alternative buffer materials is widespread and we have two atomic layer deposition (ALD) reactors for the fabrication of such layers. In this thesis the types of layers fabricated were $\text{Zn}_{1-x}\text{Mg}_x\text{O}$ in Papers I, II and III and $\text{ZnO}_{1-y}\text{S}_y$ in Papers I and VII. In Paper I the $\text{ZnO}_{1-y}\text{S}_y$ is deposited on absorbers from the UMS system while $\text{Zn}_{1-x}\text{Mg}_x\text{O}$ is deposited on BAK absorbers. The processing of $\text{Zn}_{1-x}\text{Mg}_x\text{O}$ is described in [72] while $\text{ZnO}_{1-y}\text{S}_y$ deposition in the ALD reactor is presented in [49]. The compositions of the films are determined from the frequency of precursor cycles for the constituent materials. When denoting a deposited layer as (Zn,Mg)O 1:6, it means that for every Mg-precursor cycle there are six Zn-precursor cycles in the deposition run.

The next step is to deposit the transparent front contact. This we normally do by sputtering a thin layer of undoped ZnO (i-ZnO in Figure 1.2) followed

by a thicker layer of Al-doped ZnO [30]. We complete our test devices by evaporating layered Ni/Al/Ni front contacts on top of the ZnO [30].

1.3 Aim of Thesis

The aim of my thesis is to improve the understanding on how individual layers impact the performance of CIGS solar cell devices. An important goal is to understand which material parameters limit the efficiency of the solar cells. My focus lies in particular on the properties of the absorber-buffer region. Standard devices with CdS buffer layers as well as cells with alternative buffer layers are studied. For this purpose electrical device modelling is used. Data from electrical and optical characterization are along with literature data utilized to develop device models. Each model is evaluated by comparing the output of simulations with electrical measurement results. If a credible electrical device model is accomplished a deeper knowledge on the limitations of the solar cells can be gained.

Chapter 2 contains descriptions of the characterization methods used while an overview of how the models were developed is found in Chapter 3. Results of the measurements and simulations are related in Chapter 4. Finally in Chapter 5 some conclusions are drawn on the contents of this thesis.

2. Characterization Methods

Characterization of finished CIGS solar cell devices and individual layers are important elements of this thesis. The results of these measurements may serve as input to device models. In this chapter I present a number of different characterization methods that are important for this work. Simultaneously the experimental setups are described.

2.1 Current-Voltage Measurements

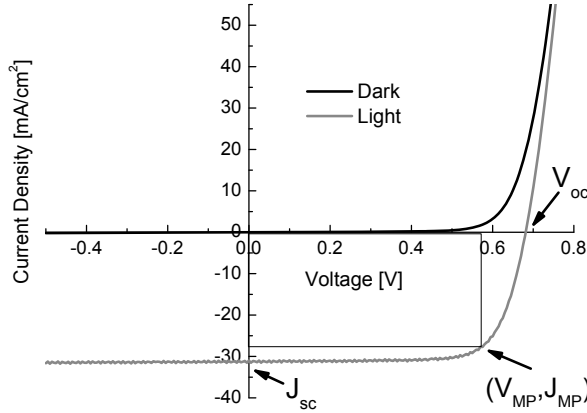


Figure 2.1: Example of current-voltage (JV) curves of a CIGS solar cell, measured in darkness and in illumination.

An essential method of characterization is to measure JV curves. From measurements in light the standard solar cell parameters that determine the efficiency of a solar cell can be obtained. These are the fill factor (FF), the open circuit voltage (V_{oc}) and the short-circuit current density (J_{sc}). V_{oc} and J_{sc} are located where the light JV curve crosses the coordinate axes as indicated in Figure 2.1. In this figure the maximum power point is indicated as (V_{MP}, J_{MP}) . The FF is a measure on how square the JV curve is and can be calculated from Equation 2.1

$$FF = \frac{J_{MP}V_{MP}}{J_{sc}V_{oc}} \quad (2.1)$$

Solar cell efficiency is defined as the output at the maximum power point divided by the power of the light directed on the solar cell (P_{in}). Equation 2.2 displays how the efficiency, η can be expressed in terms of the other parameters.

$$\eta = \frac{J_{sc}V_{oc}FF}{P_{in}} \quad (2.2)$$

2.1.1 JV Measurement Setup

For determination of the efficiency of solar cells a standard test condition (STC) is defined. Under these conditions light measurements are conducted at a temperature of 25°C using a standardized AM 1.5 solar spectrum. This spectrum has an irradiated power of 1 kW m⁻² and is shown in Figure 2.2.a). Tests of solar cells are however normally done using a solar simulator with a spectrum that differs considerably from AM 1.5. Such simulators need to be calibrated in order to measure a current similar to what would be measured in STC.

In this work we employ two different solar simulators. One of the setups uses an ELH halogen lamp equipped with a cold mirror as a light source while in the other setup, samples are illuminated by a Newport Oriel Sol2A solar simulator. Spectra of the light sources are shown in Figure 2.2.a). The first mentioned setup is employed in Papers I, II and IV-VI while the Sol2A simulator is used in Paper VII. Both setups are calibrated using a Si-photodiode with a known J_{sc} under the AM 1.5 spectrum. This is done by adjusting the light intensity until the same J_{sc} is obtained in the measurement setup. In the ELH-setup the lamp distance to the sample is changed while for the Sol2A the input power to the lamp is adjusted. Standard JV-measurements are conducted at 25°C. To avoid heating by the lamp, samples are placed on a Peltier cooler.

If the spectral response of the test cell differs from the calibration cell, as it frequently does, JV measurements will not give the correct J_{sc} -values. Better current values can be obtained by quantum efficiency (QE) measurements (see Section 2.2) on a test cell and then using this cell to calibrate the intensity of the JV light-source. This is done in Paper VII.

By comparing light-JV curves to JV-measurements in darkness one may obtain important information regarding light-induced effects such as voltage-dependent current collection or light-modulated barriers, in the studied solar cell.

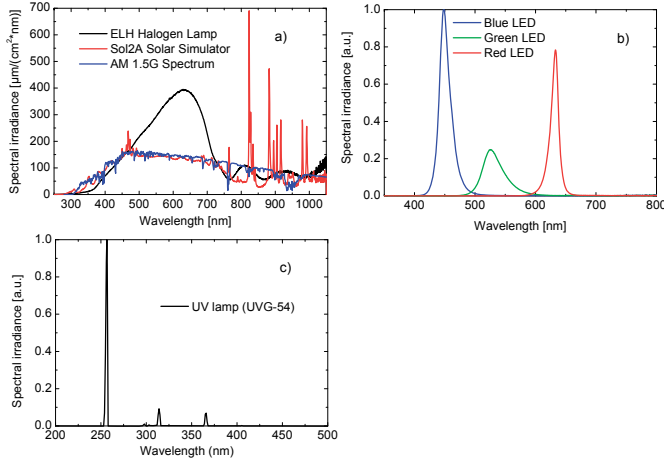


Figure 2.2: Spectra of different light-sources used in this thesis shown alongside the AM 1.5 global standard spectrum.

2.1.2 Light Soaking

CIGS solar cells often change their properties under illumination. Therefore some minutes of illumination (aka light-soaking (LS)) prior to JV-characterization is a common practice. Here the LS behaviour of CIGS solar cells with $\text{Zn}_{1-x}\text{Mg}_x\text{O}$ buffer layers is studied using several different light sources. An ELH halogen lamp and a 254nm filtered ultra-violet (UV) lamp (UVG-54) are applied in Paper II and Paper VI, respectively. Spectra of these light sources are found in Figure 2.2. LS was performed at room temperature (RT). Since the halogen lamp heats the sample significantly, a Peltier cooler was used to control temperature during LS with this lamp.

Relaxation of $\text{Zn}_{1-x}\text{Mg}_x\text{O}$ thin-films and cells with $\text{Zn}_{1-x}\text{Mg}_x\text{O}$ buffer layers was performed in darkness at RT and at elevated temperature (mainly at 370K). In Paper III results on film relaxation were presented. More results on how the cell parameters change during relaxation will be shown in Section 4.2.4. Red, green and blue light-emitting diodes (LEDs) were utilized to study the effect of LS at different wavelengths. These LEDs have dominant wavelengths (energies) of 622nm (1.99eV), 533nm (2.33eV) and 460nm (2.70eV), respectively. Spectra are shown in Figure 2.2.b). The green and blue ones have a maximum power dissipation of 1.6 W each, while the red LED has a maximum power dissipation of 1.2 W. In Section 4.2.4 unpublished results on light-soaking $\text{Zn}_{1-x}\text{Mg}_x\text{O}$ cells with these LEDs, will be presented.

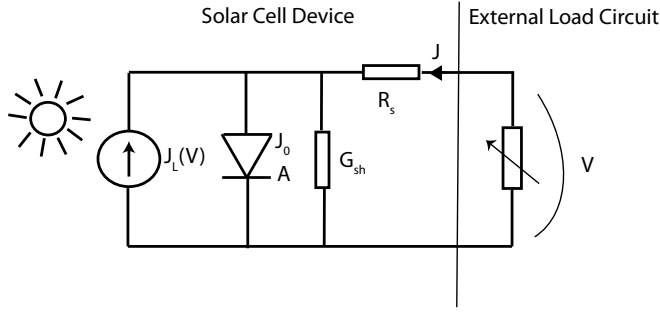


Figure 2.3: Equivalent circuit of a solar cell under illumination, according to the one-diode model.

2.1.3 One-Diode Model

The JV-characteristics of a solar cell can ideally be modelled with the equivalent circuit shown in Figure 2.3. In this circuit $J_L(V)$ represents the voltage dependent light-generated current while the other parameters are the saturation current density (J_0), the ideality factor (A), the series resistance (R_s) and the shunt conductance (G_{sh}). Equation 2.3 displays the current-voltage dependence of this circuit.

$$J = J_0 \left(\exp \left(\frac{q(V - JR_s)}{AkT} \right) - 1 \right) + G_{sh}(V - JR_s) - J_L \quad (2.3)$$

One-diode parameters can be obtained from the JV-curves by different fitting methods. In Paper II a weighted least squares method was used where all parameters are evaluated at once [40]. In Papers V-VII a method proposed by Hegedus et. al. [24] for evaluating the parameters step by step was applied. This method of evaluation gives good control and reliable results. In Paper IV-VII fitted series resistance values are used as input in simulations of JV-curves in SCAPS.

2.1.4 Characterization at Different Temperatures

From temperature-dependent JV (JVT) measurements the recombination path that limits V_{oc} can be determined. JV-curves obtained in light and in darkness can be studied with this aim. In this analysis G_{sh} and R_s are neglected. Furthermore, it is assumed that J_0 can be modelled as a product of a temperature-dependent exponential and a relatively temperature-independent prefactor, J_{00} . For $V \gg kT/q$ Equation 2.3 can then be rewritten as Equation 2.4.

$$J = J_0 \exp \left(\frac{qV - E_a}{AkT} \right) - J_L \quad (2.4)$$

In this expression the activation energy (E_a) is a parameter that is dependent on the dominating recombination path. For recombination in the space-charge region and in the neutral bulk as well as at the back contact it is equal to the CIGS band gap. If recombination at the CIGS/buffer interface dominates then E_a is equal to the hole barrier for interface recombination (ϕ_b^p). This barrier is normally lower than the CIGS band gap [58].

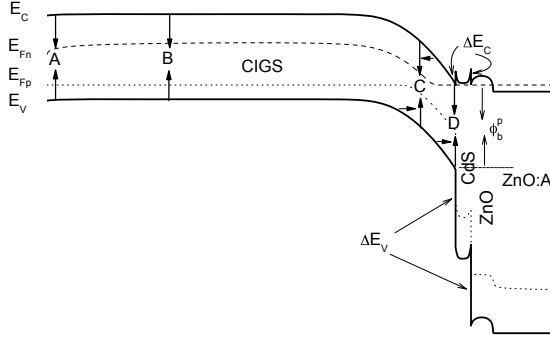


Figure 2.4: Overview of important recombination paths in a CIGS solar cell. This diagram shows a cell with ungraded band gap. Path A represents recombination at the back contact, B in the neutral CIGS bulk, C in the depletion region of the CIGS layer and D recombination at the CIGS/CdS interface. In the depletion region carrier tunnelling may enhance recombination, as indicated by arrows. Conduction band offsets are indicated by ΔE_C while ΔE_V indicates valence band offsets. In this case the conduction band offset between the absorber and buffer layers is positive, which suppresses interface recombination. E_{Fn} and E_{Fp} are the quasi-Fermi levels for electrons and holes respectively.

The different recombination paths are outlined in the band diagram Figure 2.4. Under illumination the activation energy can be determined by extrapolating V_{oc} to 0K. Assuming that E_a is linearly dependent with temperature Equation 2.4 can be rewritten into Equation 2.5 when $V=V_{oc}$ and $J=0$.

$$V_{oc} = \frac{E_a^0}{q} + \frac{kT}{q} \left(C - A \ln \left(\frac{J_L}{J_0} \right) \right) \quad (2.5)$$

Another method to determine E_a is to plot $\ln J_0$ versus $1/kT$. Then the activation energy is obtained as the slope of a linear fit to these data. We apply these two methods to determine E_a in all papers where JVT analysis was performed (I,II,V and VII). A third method, where E_a is obtained from a non-linear least squares fit to A and $1/kT$ data is used in Papers I and II. Further discussion on these methods can be found in Paper II and in a paper by Malm and co-workers [40].

Whether the ideality factor is temperature-dependent or not and how it in that case varies depends on many factors such as the dominating recombination path, the presence of tunnelling-enhancement, the distribution of defects in the band-gap and if the Fermi-level is pinned or not [41, 56, 58, 61]. We tested and evaluated two models on the temperature-dependence of A . These models are discussed in Paper II.

All of the JVT measurements in this thesis are performed in a cryostat cooled with liquid nitrogen. Measurements were performed both in darkness (with the shutter closed) and in light (with the shutter open). An ELH-halogen lamp was used for illumination. Similarly to above, the light intensity is calibrated by varying the height of the lamp and checking J_{sc} . In Paper II white LS of the samples was performed at room temperature prior to measurements.

There were a number of complications when analysing the recorded measurement data. In Papers I and II it was problematic to fit the JV-curves of CGS and CIGS cells with ALD buffer layers to the one-diode model, without previous light-soaking. Even after light-soaking, light JV curves of cells with Mg-rich $Zn_{1-x}Mg_xO$ buffer layers obtained at low temperatures could not be reasonably fitted in Paper II. For the CGS-devices in Paper I with $Zn_{1-x}Mg_xO$ buffers only JV-curves down to 260 K could be fitted.

In many cases the two models describing the temperature-dependence of the ideality factor fitted equally well or poorly to the ideality factors extracted from JVT measurements. This is especially common for cells with alternative buffer layers. The reason for this could be that none of the models are applicable for these devices. As already mentioned a number of assumptions are necessary when deriving the evaluated models [56, 58]. Another explanation might be that the amount of recombination in the depletion region and at the interface is on a similar order of magnitude in these devices. These issues are further discussed in Paper II.

2.2 Quantum-Efficiency Measurements

The external quantum efficiency (EQE) is defined as the average number of electron-hole pairs that are collected for each photon directed on the solar cell. This property varies with the wavelength of the incoming photons and therefore it is measured using monochromatic light. The wavelength of the monochromatic light is varied within the range of interest. An example of

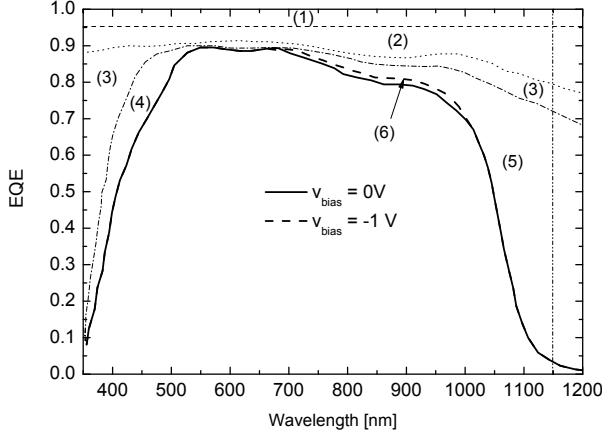


Figure 2.5: An overview of J_{sc} losses and how these can affect an external quantum efficiency curve of a CIGS solar cell. Loss (1) represents shading from the front grid while (2) is the loss due to reflection of light from the CIGS device structure. The areas (3) and (4) are losses caused by the light absorption in the doped ZnO window and CdS layers, respectively. The loss due to incomplete generation in the CIGS is indicated by (5) while the difference between zero bias and -1 V QE curves, (6), is the loss due to voltage dependent current collection. Plotted data are taken from [67]

an EQE-curve of a CIGS solar cell is shown in Figure 2.5. EQE curves are affected by various current loss mechanisms in different wavelength ranges. Figure 2.5 contains an overview of such losses. We measure EQE using light directed at spots on the cells not covered by grid. This means that loss (1) in the figure does not affect our measured EQE curves. By integrating an EQE curve with the AM1.5 solar spectrum we can obtain J_{sc} in STC. We must however also correct the current value downwards by considering the grid area that would be illuminated when measured in STC.

If the reflectance of the cell is measured as a function of photon wavelength one may calculate the internal quantum efficiency (IQE) from the EQE using Equation 2.6.

$$IQE(\lambda) = \frac{EQE(\lambda)}{1 - R(\lambda)} \quad (2.6)$$

IQE is a measure of the fraction of generated electron-hole pairs that is collected at the contacts.

In this thesis EQE-measurements were conducted using two different setups. One existing setup and one which I participated in building up. In Papers I and II we employed our old setup while in the rest of the thesis we used the new one. Both QE-equipments are built on the same principles but with some

differences in the design. In both cases a Xe-arc lamp is used as light source. Light passes through a monochromator and a chopper and is then directed onto the solar cell which results in an electrical signal from the cell. One part of the monochromatic beam is directed on a reference cell that monitors the lamp intensity. To discriminate the wanted alternating current (AC)-signal, having the chopping frequency, from the direct current (DC) or AC background noise, the measurement and reference signals are processed in lock-in amplifiers. The chopping frequencies are 78 Hz and 70 Hz in the old and new setup, respectively. As reference cells sandwiched Si/Ge (old) and Si/InGaAs (new) photodiodes are used in the respective equipments. A further difference is that the old setup contains a glass fiber cable for light direction while in the new setup mirrors and lenses serve this purpose. To calibrate the QE-measurements separate photodiodes with known spectral responses were applied. For calibration of the old equipment Si and Ge diodes were applied while for the new setup Si and InGaAs diodes were used.

On standard CIGS solar cells QE-measurements with and without light-bias usually give similar results. Most measurements in this thesis were performed under ambient light conditions. However for more non-ideal devices, differences are common. ELH-lamp biased measurements were conducted on CGS in Paper I.

In the new equipment there is also a possibility to apply a voltage-bias on the measured sample. We used this feature in Papers V-VII.

2.3 Capacitance-Voltage Profiling

In capacitance-voltage (CV) profiling the effect of applying an AC signal on dc-biased p-n or Schottky junctions is studied. The capacitance of the junction is obtained from the measured complex admittance (Y). In our analysis we assume that the junction can be modelled by a shunt resistance and a capacitance in parallel. This is valid if the series resistance in the measurement is small. In that case the capacitance is roughly equal to $\text{Im}(Y)/\omega$ where ω is the AC frequency [22].

CV measurements on diodes are normally analysed using the depletion approximation. According to this approximation the capacitance response of the junction originates solely from the edge of the depletion region which means that the junction is modelled as a plate capacitor. The depletion width of a plate capacitor is given by Equation 2.7 [71].

$$W = \frac{A\epsilon}{C} \quad (2.7)$$

Assuming that the measured sample is an abrupt p-n⁺ junction, Equation 2.8 gives the relation between the capacitance and the doping at the edge of the p-side depletion region (N_A) [22, 71].

$$\frac{1}{C^2} = -\frac{2(V_{bi} - V_{dc})}{q\epsilon A^2 N_A} \quad (2.8)$$

Here ϵ is the permittivity of the p-side semiconductor, V_{bi} is the junction built-in voltage while V_{dc} is the applied DC voltage.

To study the doping profile the bias voltage is swept within an appropriate range. Ideally a so called Mott-Schottky plot of $1/C^2$ against the DC bias voltage should be linear, if the doping is constant with depth in the sample, but in reality various deep defects and interface states might influence the result. Examples of Mott-Schottky plots of a CIGS device, obtained in a range of temperatures, are shown in Figure 2.6. For each bias voltage the doping at the edge of the depletion region ideally can be calculated from Equation 2.9 [22, 71].

$$N_A = -\frac{C^3}{q\epsilon A^2} (dC/dV)^{-1} \quad (2.9)$$

In our work N_A and ϵ_s represent the doping and permittivity of the CIGS layer. To get the position dependence, the doping for each CV measurement is plotted as a function of the depletion width calculated at the corresponding voltage using Equation 2.7.

One thing that complicates CV profiling of thin film semiconductors is the large concentration of deep trap states with different activation energies. These states affect the capacitance both by modifying the space charge density and thereby the depletion width and by changing state at the depletion edge, following the AC-voltage. This makes it difficult to measure the true doping profile using CV. To reduce the effects of the deep states one can conduct the measurements at high frequency and low temperature [22]. Example of apparent doping profiles of a CIGS solar cell are shown in Figure 2.7. These plots are based on the same measurement data as Figure 2.6.

We performed the CV measurements of Papers V and VII in darkness in the same liquid nitrogen cooled cryostat as we used for JVT measurements. CV-profiles of CIGS solar cell devices were recorded from 150 K and upwards with the DC-voltage sweep running between 1 V and -2 V. We applied an AC-signal with a frequency of 500 kHz and an amplitude of 30 mV on each sample. An LCR-meter was used for capacitance measurements. In the analysis we assumed a CIGS relative permittivity of 13.

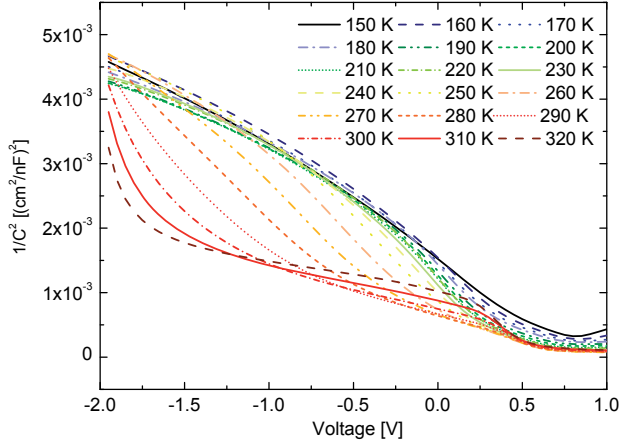


Figure 2.6: Mott-Schottky plots of a CIGS solar cell with a CdS buffer layer, acquired at a sequence of temperatures.

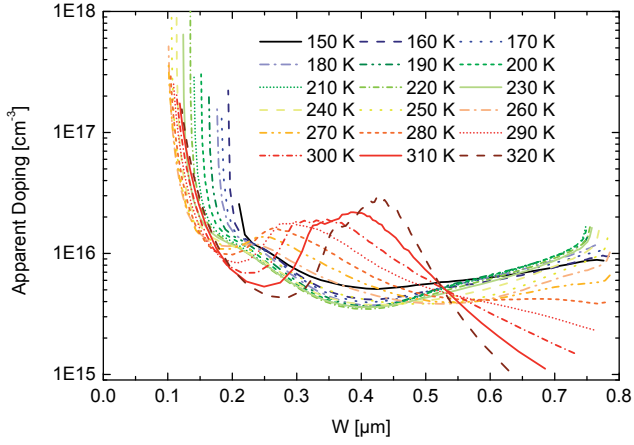


Figure 2.7: Apparent doping profiles of a CIGS solar cell with a CdS buffer layer calculated from CV measurements at a sequence of temperatures.

2.4 Resistivity and Hall Measurements

2.4.1 Four-Point Probe Measurements

An established technique to measure the resistivity of a thin film is to apply a four-point probe on the sample surface. In this technique a voltage is applied over two of the contacts while the current is measured between the other two contacts. In this way the effect of the wire and contact resistances on the measurements can be eliminated [66]. In Papers III and VI we conducted four-point resistivity measurements with probes arranged in a square shape. The resistivity (ρ) can for our geometry be calculated from the applied voltage and resulting current using Equation 2.10, where t is the film thickness.

$$\rho = 9.06 \frac{Vt}{I} \quad (2.10)$$

This expression is valid if the probes are positioned far away from the edges relative to the distance between the probes.

2.4.2 Hall Effect Measurements

By measuring the Hall effect in a semiconductor one may obtain the mobility and the free carrier density of the material in addition to the resistivity. Also whether the sample is of n-type or p-type conductivity can be determined.

The origin of the Hall effect is the force that acts on electrons that move perpendicular to a magnetic field. This force sets up the so called Hall voltage (V_H) in the direction perpendicular to the magnetic field and the current. This voltage is included in the definition of the Hall coefficient (R_H) [66].

$$R_H = \frac{tV_H}{BI} \quad (2.11)$$

In Equation 2.11 the assumption is that the magnetic field is perpendicular to the film surface. The sign of R_H will be different depending on if the conduction in the films is due to holes or electrons. Therefore the carrier density is given by one or the other of the following expressions [66].

$$p = \frac{1}{qR_H} ; n = -\frac{1}{qR_H} \quad (2.12)$$

If both carrier types contribute to the conduction the situation is more complicated. For simplicity energy-independent carrier scattering mechanisms is assumed when deriving Equation 2.12. This simplification is usually done when evaluating thin films [46]. The majority carrier mobility is then calculated from Equation 2.13.

$$\mu = \frac{|R_H|}{\rho} \quad (2.13)$$

We use the the so called Van der Pauw method to evaluate the carrier density and mobility of the $\text{Zn}_{1-x}\text{Mg}_x\text{O}/\text{SLG}$ glass samples of Paper III. In this technique the films should be uniformly thick and not include any isolated holes. The contacts should be ohmic, sufficiently small and positioned at the circumference of the sample [46]. Our samples are square-shaped with soldered In-dots at the corners. In the Van der Pauw-method a number of resistance measurements are made. For each measurement the current is driven between two contacts while the voltage simultaneously is measured at the two other contacts. For resistivity determination, measurements are made between neighbouring contacts without magnetic field. Carrier density and mobility are calculated from measurements between opposite contacts with magnetic field applied [45, 66]. We apply a magnetic field of 0.4T through our samples. In order to eliminate any thermo-electric voltage that could appear due to nonuniform sample temperature, each measurement is conducted for both current directions. To avoid any errors caused by misaligned contacts, measurements are performed both with positive and negative magnetic field direction [54].

2.5 CIGS Compositional Analysis

We use x-ray fluorescence (XRF) in Papers I, II, V and VII to determine the average depth composition of our deposited CIGS layers. In this method a primary X-ray beam is directed on the sample where it excites core electrons. This excitation is followed by emission of secondary x-rays with energies characteristic for each element, when electrons relax into the empty core orbitals. Our measurements were performed in a SPECTRO X-LAB 2000 system that contains a semiconductor sensor for X-ray detection. Each measurement is recorded over a circular sample area with a diameter of 1 cm. A standard sample of known composition was used for calibration.

To determine the CIGS-composition as a function of depth, two different methods were applied. For the compositional profiles utilized when modelling devices in Papers IV, V and VI we applied secondary ion mass spectrometry (SIMS) while for the profiles of Paper VII we used x-ray photoelectron spectroscopy (XPS) and sputtering.

In XPS a monochromatic $\text{Al K}\alpha$ (1.487keV) x-ray beam is directed onto the sample. Due to the photoelectric effect, electrons gain enough energy to leave the sample. This technique is highly surface sensitive since the electrons have a short penetration depth in a solid material. By measuring the kinetic energies of the emitted electrons, peaks associated with element specific bind-

ing energies in the sample can be identified. From these binding energies the composition at the sample surface may be deduced. To obtain depth compositional profiles, Ar^+ ion sputtering was applied in between the acquisition of XPS data. Measurement data from an area with a diameter of $150\mu\text{m}$ was collected. Calibration of sensitivity factors, taking into account preferential sputtering effects, was performed by measuring the same profile on a non-graded CIGS sample with metal composition determined by XRF.

SIMS also involves sputtering of the sample under study with the aim of determining the composition at different depths. In SIMS however, the composition is determined by measuring the rates of different ion species sputtered from the sample in a mass spectrometer. The SIMS system we have used, utilizes Cs^+ ions for sputtering and detects molecular MCs^+ ions in order to reduce the effect of a varying chemical environment of a studied atom species [20]. The SIMS data is collected from an area having a diameter of $60\mu\text{m}$. SIMS compositional data were calibrated using the average GGI ratio from XRF. More details on SIMS and analysis of measurement data are found in a previous thesis from our group [62].

A comparison of different methods for analysing thin film composition as a function of depth was carried out by Abou-Ras and co-workers [2]. They obtained similar Ga/III (GGI) profiles from XPS and SIMS.

2.6 Optical Characterization

Optical reflection and transmission measurements are valuable tools for characterizing individual layers as well as the solar cell as a whole. In Paper III we use reflection and transmission data to determine the band gaps and absorption coefficients of the processed $\text{Zn}_{1-x}\text{Mg}_x\text{O}$ thin films while in Papers IV and VII we measure the reflectance as a function of wavelength of finished (apart from front contact grid) solar cell stacks.

The absorption coefficients are used as input data for light absorption in SCAPS. Additionally, they are utilized to determine band gaps of the thin films. There are a number of different methods for doing this but we use the common approximation given in Equation 2.14 [41] where absorption coefficients, $\alpha(\lambda)$, are calculated from the reflectance, R , and the transmittance, T .

$$\alpha(\lambda) = -\frac{1}{d} \ln \left(\frac{T(\lambda)}{(1 - R(\lambda))^2} \right) \quad (2.14)$$

For direct band gap materials such as $\text{Zn}_{1-x}\text{Mg}_x\text{O}$ [72] the band gap can be obtained by linear fitting of a plot of the square of the absorption coefficient to the photon energy [70]. The band gap energy is found where the fitted line intercepts the energy-axis.

All reflection and transmission measurements were conducted in the same setup. This system includes a light source, a monochromator and a Perkin-Elmer λ 900 dual beam spectrophotometer equipped with an integrating sphere. The purpose of such a sphere is to collect both diffusely and specularly transmitted and reflected light. In this thesis the wavelength range between 300nm and 1500nm, which includes the wavelengths important for CIGS solar cells, is investigated.

3. Electrical Modelling and Simulations

The main topic of this thesis is electrical modelling and simulations of solar cell devices. In order to simulate the cell behaviour in a realistic way a credible electrical model must be elaborated. In this chapter I will first give a short introduction to the theory underlying electrical simulations of solar cells. Subsequently the software that I used in the work will be presented. Finally in Section 3.3 a discussion on the material parameters used in the simulations will follow.

3.1 Basic Equations

The fundamental differential equations for semiconductor device modelling are Poisson's equation and the steady-state continuity equations for electrons and holes (Equations 3.1-3.3).

$$\nabla(\epsilon \nabla \Psi) = q(p - n + N_D^+ - N_A^-) \quad (3.1)$$

$$\nabla \cdot \mathbf{J}_n = -q(G - R_n) \quad (3.2)$$

$$\nabla \cdot \mathbf{J}_p = q(G - R_p) \quad (3.3)$$

In these equations Ψ is the electric potential, n and p are the carrier densities, ϵ is the permittivity of the semiconductor, N_D^+ and N_A^- are the densities of ionized donors and acceptors, \mathbf{J}_n and \mathbf{J}_p are the electron and hole current densities while G , R_n and R_p are the carrier generation and recombination rates. Poisson's equation is one of Maxwell's equations, while the continuity equations (3.2 and 3.3) ensure conservation of charge, in other words that the net current flow from a small volume equals the net generation of charge carriers there. When solving these equations appropriate boundary equations are necessary.

Another important set of equations are the transport equations describing the current flow. The basic form of Equations 3.4 and 3.5 is commonly used for semiconductors. The first term in this equation is due to drift in an electric

field while the second one is the diffusion term due to carrier concentration gradients

$$\mathbf{J}_n = q\mu_n n \nabla \Psi + qD_n \nabla n \quad (3.4)$$

$$\mathbf{J}_p = q\mu_p p \nabla \Psi - qD_p \nabla p \quad (3.5)$$

Here μ_n , μ_p , D_n and D_p represent mobilities and diffusion coefficients of the different carrier species. There might also be other sources of current transport to consider, such as tunnelling or gradients in various physical properties, e.g. in temperature, band gap, band density of states and electron affinity [16].

3.2 Modelling Software

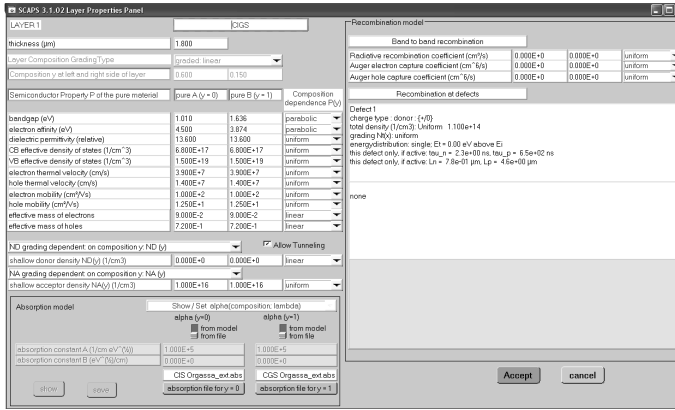


Figure 3.1: Screenshot from SCAPS 3.1 showing the layer properties panel.

The software that is almost exclusively used in this thesis is called SCAPS [9]. This program numerically solves more elaborate versions of the fundamental differential equations of Section 3.1, in one dimension. To determine the occupancy of bands and defect states Maxwell-Boltzmann statistics is applied. This approximation of Fermi-Dirac statistics is valid when the Fermi-level is within the band gap and not closer than kT to a band edge, that means not for very highly doped semiconductors. Current transport in SCAPS accounts for the influence of grading in the material properties as well as intra-band tunnelling and tunnelling to and from defects [8, 73]. JV, CV, QE as well as C-f measurements can be simulated using this application.

A great number of electrical parameters can be set for each layer in the structure. In Figure 3.1 a screenshot shows the appearance of the layer prop-

erties panel, where this setting is done. This figure shows a graded CIGS layer where the two manually entered values are for the two extreme compositions. In this case these end points represent pure CIS and CGS. Most material parameters can be chosen graded, with some functional dependence on composition. The composition can in itself be graded with position. Defects of various types can be defined, both in the bulk of layers and at interfaces. Optical properties such as absorption coefficients and front and back-side reflections, as functions of wavelength, can be imported from text-files. Reflection at other interfaces are however not handled by SCAPS. Absorption coefficients are interpolated internally between the defined extremum compositions [8].

During the course of my work I also used a few other applications for device modelling. These are PC1D [12], commonly used to model crystalline Si-solar cells and AFORS-HET [17], developed for heterojunction solar cells. Both model devices in one dimension. Furthermore I have tested ATLAS [69] that facilitates simulations in two and three dimensions.

3.3 Parameter Selection

Since an electrical device model of a CIGS solar cell is dependent on a large number of parameters, it is worth to give an extensive discussion here on how to select these. A complication is that many of the parameters are largely unknown for the modelled devices. As a first step in achieving a baseline parameter set for cells with CdS buffer layers, I performed a literature study of previous work done on CIGS device modelling. With these data as a starting point we developed the baseline set by fitting simulation results to measurements.

The baseline parameters and resulting JV- and QE-curves were first presented in Paper IV. The parameter set is shown once more, though with a few modifications, in this thesis. In this section I will discuss some aspects on the parameter selection one layer at a time. Parameters used for the alternative buffer layers are a central part of the results of this thesis. These parameters will be discussed in Section 4.2.

3.3.1 Modelling Parameters

Table 3.1 is based on the parameter set of Paper IV but with a few changes, most of them mentioned in Paper VI. In Paper VI a baseline set without surface defect layer (SDL) was described (see Section 3.3.6.1 for an introduction to the SDL). Parameters of this model that differ from those of the model including SDL are shown within parentheses. All layers are polycrystalline and therefore contain a large number of different defects which may be process dependent. This is especially true for the CIGS layer [77]. As done by some authors previously we for simplicity position all bulk defects at mid gap of the

respective layers [19, 42]. Likewise, interface defects are placed at midgap of the neighbouring material with the lowest band gap. Defect cross-sections are mainly based on literature as is discussed in Paper IV.

3.3.2 Back Contact

It has been observed that there exists a thin MoSe₂ layer in high-efficiency CIGS cells between the molybdenum back contact and the absorber layer [44]. This layer has been considered to give a slight Schottky barrier for holes towards the molybdenum. This barrier was suggested to be thin enough not to show up in room temperature JV-curves [58]. Later studies have found that CIGS/MoSe₂/Mo and CGS/MoSe₂/Mo contacts behave ohmic, also at low temperatures [5, 32, 74]. MoSe₂ can however grow either in the perpendicular or the parallel direction towards the substrate depending on the choice of CIGS process. The electrical properties will depend on growth direction [3, 74]. Parallel oriented MoSe₂ may induce a high series resistance [10]. The growth direction is dependent on various process parameters such as the presence of Na [3, 10]. This means that the electrical properties of the back contact are process dependent. In all of our papers, except one, we assumed an ohmic back contact. In Paper VII however, we introduced a low Schottky hole barrier. No reflection at the back contact was assumed.

3.3.3 CIGS Absorber Layer

The CIGS absorber doping in the papers is based on a combination of references, own CV-measurements and fits to JV and QE measurement data. We also took the recombination path limiting V_{oc} determined from JVT-analysis into consideration.

Compositional grading and the resulting band gap grading was in Papers IV-VI determined by XRF and SIMS while in Paper VII XRF and XPS were used. In all papers we approximated the compositional gradings by linear and parabolic functions. See Figure 4.13 for a visual presentation of the compositional profiles used in simulations. Band gap values were calculated from the GGI ratio according to Equation 3.6 [4, 67].

$$E_g = 1.01 + 0.626 * GGI - 0.167 * GGI * (1 - GGI) \quad (3.6)$$

Deep defect density and electron mobility were selected by fitting to JV and QE experimental data with the side condition that the electron diffusion length should have a reasonable value on the order of one μm . All other parameters are to a large extent based on literature. More on the parameter selection, including references, is found in Paper IV.

Table 3.1: *Baseline parameter set for modelling CIGS solar cells with MrPilote CIGS and chemical bath deposited CdS buffer layers. Parameter values unique for the model without SDL included in parentheses. In connection to defect densities, (a) and (d) denote shallow acceptor and donor defects while (A) and (D) denote deep acceptor and donor defects.*

	Layer Properties			
	CIGS	SDL	CdS	Doped ZnO
Thickness [μm]	1.8	0.015	0.05 (0.07)	0.08
E_g [eV]	Graded	1.33	2.4	3.3
ϵ_r	13.6	13.6	5.4	9
N_C [cm^{-3}]	6.8×10^{17}	6.8×10^{17}	1.3×10^{18}	3×10^{18}
N_V [cm^{-3}]	1.5×10^{19}	1.5×10^{19}	9.1×10^{18}	1.7×10^{19}
v_{th}^n [cm/s]	3.9×10^7	3.9×10^7	3.1×10^7	2.4×10^7
v_{th}^p [cm/s]	1.4×10^7	1.4×10^7	1.6×10^7	1.3×10^7
μ_n [cm^2/Vs]	100	10	72	100
μ_p [cm^2/Vs]	12.5	1.25	20	31
Doping [cm^{-3}]	10^{16} (a)	10^{16} (a)	5×10^{17} (d)	1.1×10^{16} (d)
Bulk Defect Properties				
N [cm^{-3}]	1.1×10^{14} (D)	1.1×10^{14} (D)	5×10^{16} (A)	10^{16} (A)
σ_n [cm^2]	10^{-13}	10^{-13}	10^{-15}	10^{-15}
σ_p [cm^2]	10^{-15}	10^{-15}	5×10^{-13}	5×10^{-13}
Interface Properties				
	CIGS/SDL	SDL(CIGS)/CdS		CdS/Undoped ZnO
CBO [eV]	0.0	0.0		-0.2
N [cm^{-2}]	10^9 (D)	3×10^{13} (10^{11}) (D)		-
σ_n [cm^2]	10^{-13}	10^{-13}		-
σ_p [cm^2]	10^{-15}	10^{-15}		-

3.3.4 CdS Buffer Layer

CdS doping and defect density values were chosen based on literature and fitting to JV and QE data. The net doping affects the amount of interface recombination in the cell which means that also here the JVT-analysis must be regarded. The thickness of the deposited CdS has some variation and may therefore within a reasonable range be fitted to the QE-curve.

3.3.5 Window Layer

For the undoped and Al-doped ZnO layers mostly literature data was used. When selecting the electron mobilities and net doping densities however, a side condition should be that the resistivity calculated from these is reasonably similar to the resistivity that we measure using four-point probe.

3.3.6 Interface Region

3.3.6.1 Surface Defect Layer

Electrical properties of the thin defect layer at the CIGS front surface, is not so well known. It is not even clear if it exists in finished CIGS-devices. What has been measured is a wide surface band-gap on bare CIS-films [43, 63]. This layer is Cu-poor and while some authors claim it is several nanometers thick [33, 64] others claim it is a surface reconstruction, only 1-2 atomic layers in extent [38]. It has been suggested that the wide-gap SDL forms a valence band offset towards the bulk CIGS [64].

Such a layer, with a thickness of 15 nm, is included in Paper IV and in some models of Paper VI. This layer reduces interface recombination due to the wide band gap. In these papers all electrical properties of the SDL were chosen similar to the bulk CIGS except the band gap and the carrier mobilities. Lower mobilities were chosen since this layer could be more disordered than the bulk material.

Good fits to measurements on CdS cells are however obtainable also from simulations without including SDL. It is uncertain how the SDL band gap would vary with surface GGI. Therefore, to simplify the modelling, we did not include the SDL in Papers V and VII.

3.3.6.2 Conduction Band Offsets

Numerous authors have tried to determine conduction band offset (CBO) between CIS and CdS [31, 39, 43, 65]. Results have ranged from slightly negative up to 0.7 eV positive. A very high CBO would however block the current unless the CdS is very highly doped (see Fig. 4.4.d)). Most estimates were based on photoemission spectroscopy measurements of the valence band offset (VBO). An exception is [43] where also the conduction band was probed using the inverse photo-electron spectroscopy (IPES) technique. They found

a value for the CBO of (0.0 ± 0.2) eV. One thing that makes a negative offset less likely is that recombination in the depletion region normally limits V_{oc} for CdS-cells. A negative offset would enhance interface recombination and be especially detrimental if a high density of interface defects is present.

When establishing an electrical model one must also consider that the CBO is lowered when the Ga-content at the CIGS surface is raised, due to the rise in the conduction band. Slightly different CBO values were chosen in the different papers. In Paper IV a CBO of 0 eV was used based on [43], while in Paper V we introduced slightly positive CBO values based on fitting to JV and QE measurements. In Paper VII the CBO values used for the CdS-cells are in agreement with those of Paper V if one takes the different surface GGI ratios into consideration. The negative CBO between the CdS and the window ZnO layer is taken from [19].

3.3.6.3 Interface Defect Properties

Interface defect densities were obtained by fitting simulated JV and QE curves to measured ones, with the side condition that the devices with CdS buffers are not dominated by interface recombination. In Paper IV we used neutral interface defects for simplicity. In the rest of the papers donor defects were assumed, to obtain a more realistic model. Such defects will in effect also be neutral since the absorber-buffer interface region is inverted with electrons being the majority carriers. Therefore the effect on the result from this adjustment is insignificant. Fermi level pinning at the absorber-buffer interface was modelled by a high density, $3 \times 10^{13} \text{ cm}^{-2}$, of donor defects close to the CIGS conduction band. Here small capture cross-sections of 10^{-18} cm^2 were chosen to separate pinning defects from recombination defects.

3.3.6.4 Front Contact

We assumed an ohmic front contact in all papers. In Papers IV and VI we applied measured reflection data obtained on finished cell stacks as optical front contact reflection filters while in Paper V we assumed a wavelength independent reflection of 6%. This was done to better reproduce the measured EQE curves in the simulations. Since the devices of Paper V have an antireflective coating there is little optical interference and therefore the assumption of a constant reflection was sufficient. A different approach was used in Paper VII where the measured EQE curves instead were modified with the measured total reflection to obtain the internal quantum efficiencies. Simulated curves were then compared with the IQE curves calculated from measurements. In this way all optical interference could be excluded from the comparison.

4. Modelling and Measurement Results

4.1 Results of Simulations Using the Baseline Parameter Set

In this section measurement data for devices with CdS buffer layers are compared with SCAPS modelling results obtained using the baseline parameters presented in section 3.3 and Table 3.1. Figures 4.1 and 4.2 show comparisons of JV and QE curves acquired at RT, respectively. Light JV parameters from simulations and measurements are displayed in Table 4.1.

Measured JV-curves are very well reproduced by the two baseline models with and without SDL. In the QE-curves there is a slight difference between simulations and measurements at long wavelengths. From simulated curves an optical band gap of 1.13 eV is extracted while from the measurement an optical bandgap of 1.11 eV is obtained. This difference could be due to uncertainties in the shape of the SIMS profile as well as in the GGI ratio measured by XRF. The reason why the minimum bandgap of the profile used in simulations, which is 1.08 eV, is not obtained as minimum band gap in the simulated QE-curves is that the CIGS-layer is graded. This means that only a thinner portion of the absorber has this low band gap leading to incomplete absorption at photon energies close to the minimum gap. The difference in QE between the two models at wavelengths around 500 nm is mainly due to the difference in interface defect density between the models.

Table 4.1: *Measured and simulated solar cell JV-parameters for cells with CdS buffer layers. J_{sc} values are obtained from QE-measurements.*

	V_{oc} [mV]	J_{sc} [mAcm ⁻²]	FF [%]	η [%]
Measurement	646	34.0	76.1	16.7
Simulation w. SDL	655	34.2	76.1	17.0
Simulation w/o SDL	654	34.6	76.6	17.3

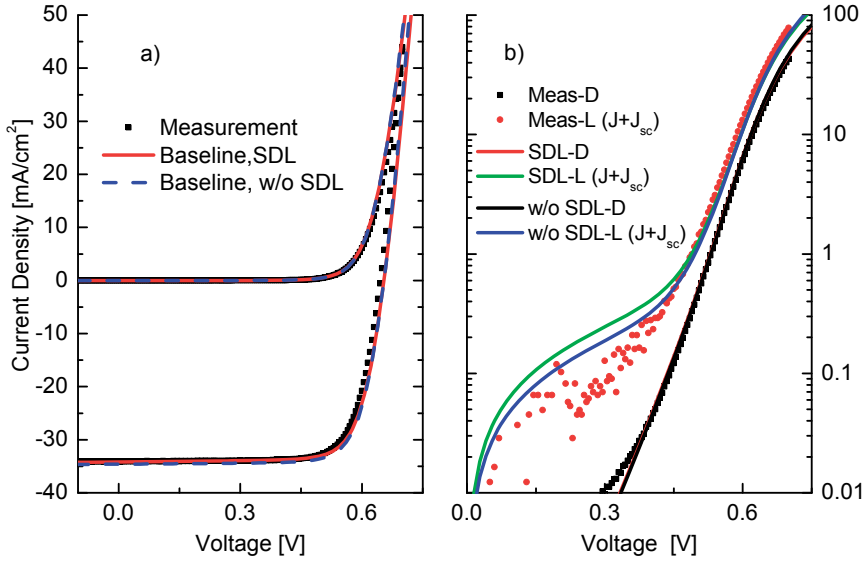


Figure 4.1: RT dark (D) and light (L) JV-curves of the baseline model with and without SDL shown alongside measurements. No Fermi-level pinning at the interface. Data shown in linear scale in a) and in semi-logarithmic scale in b). In b) light curves are shifted with J_{sc} .

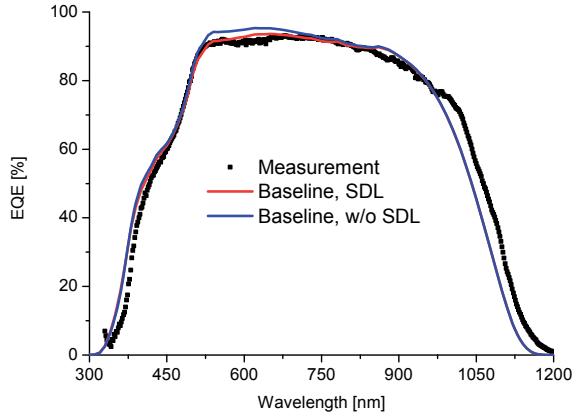


Figure 4.2: Measured and simulated external QE-curves at RT. Simulated curves are obtained without Fermi-level pinning from the baseline models with and without SDL.

4.1.1 Parameter Variations

We have performed a sensitivity analysis of the baseline parameter set. The result of this analysis is shown in a table in Paper VI. A number of absorber layer properties, such as doping and defect density, have considerable influence on the results. Also the electrical properties of the interface and the CdS doping are important. Here I will give detailed results from varying some of the more influential electrical parameters.

In Figure 4.3 the net doping densities of the buffer and the absorber are varied. The net doping is the difference between the shallow doping density and the compensating deep defect density. Baseline models with and without SDL are studied. When including Fermi-level pinning, the pinning defects, introduced in section 3.3, are positioned at the absorber-interface 0.1 eV below the lowest conduction band. In the baseline case the conduction band minimas of the buffer and the absorber are on the same level. Since the parameter variations have just minor effects on J_{sc} only graphs for V_{oc} and FF are shown.

Absorber doping variations of Figures 4.3. a) and b) include simultaneous variations of the SDL and CIGS-layer dopings when a defect layer is included. From these figures it can be deduced that V_{oc} and FF remain high as long as the net doping on the n-side is much greater than the net doping on the p-side. This means that when the absorber doping approaches $5 \times 10^{17} \text{ cm}^{-3}$ from below or when the buffer doping approaches 10^{16} cm^{-3} from above, the V_{oc} and FF drop drastically. This is true if not the Fermi-level is pinned at the interface, since the sharp drop is due to an increase in interface recombination. If E_F is pinned the V_{oc} and FF are very stable towards CdS doping variations. Due to the pinning the band bending in the CIGS is kept relatively constant even for low buffer doping and thus hole diffusion to the interface and thereby interface recombination is kept low at forward bias. In general V_{oc} and FF show a more varying response towards absorber doping variations than towards buffer doping variations. Variations at low absorber doping is due to varying amount of recombination in the CIGS-layer while at higher dopings interface recombination becomes important.

In Figure 4.4 the absorber-buffer interface donor defect density and the absorber-buffer CBO are varied. Figure 4.4.a) demonstrates that V_{oc} of the models without SDL is sensitive to a high density of mid-gap recombination interface defects. This is especially the case when there are no shallow pinning defects at this interface. Notable is the difference in response in comparison to the effect of doping variations in Figure 4.3, where the models without E_F -pinning were the more sensitive ones.

E_F -pinning counteracts the effect on V_{oc} induced by a negative CBO, by maintaining the CIGS band bending, as one can see in Figure 4.4.c). Here the Fermi-level is pinned 0.1 eV below the absorber conduction band. In Figure 4.4.d) a sharp decrease of FF is seen for CBOs higher than 0.6 eV. Such a high offset blocks the light-generated electrons from the absorber.

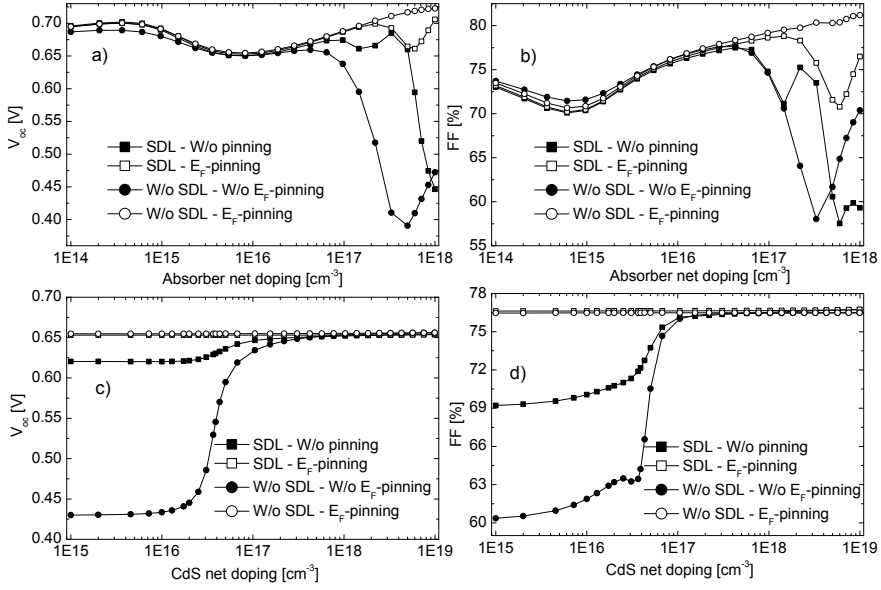


Figure 4.3: Development of V_{oc} and FF when varying the absorber and buffer net dopings in the baseline models at 300 K. Data are plotted for the situations with and without SDL as well as with and without Fermi-level pinning at the absorber-buffer interface.

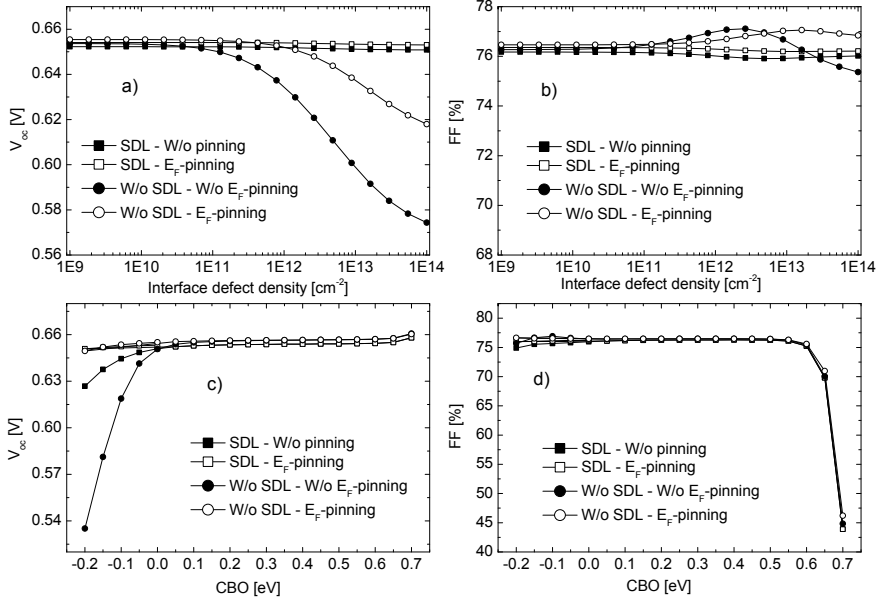


Figure 4.4: Development of V_{oc} and FF when varying the interface donor defect density and buffer-absorber CBO in the baseline models. Simulations were performed at 300 K. Data are plotted for the situations with and without SDL as well as with and without Fermi-level pinning at the absorber-buffer interface

Now I will look further into some properties of the SDL since much is uncertain regarding this layer. Thickness and band gap of the SDL are varied in Figure 4.5.a) and b), respectively. The major influence is on V_{oc} and therefore only this parameter is shown. In addition to the baseline model also a model with a hole mobility of $12.5 \text{ cm}^2/\text{Vs}$ in the SDL is shown. This is a factor ten greater than in the baseline set and equal to the hole mobility of the bulk CIGS. In both cases the situations with and without Fermi-level pinning at the absorber-buffer interface are displayed. All recombination interface defects are positioned at the intrinsic energy of the SDL (or of the CIGS layer if the SDL is absent) just as before. The left-most points in Fig. 4.5.a) are obtained without SDL but with the same absorber-buffer interface defect density as in the baseline model including SDL.

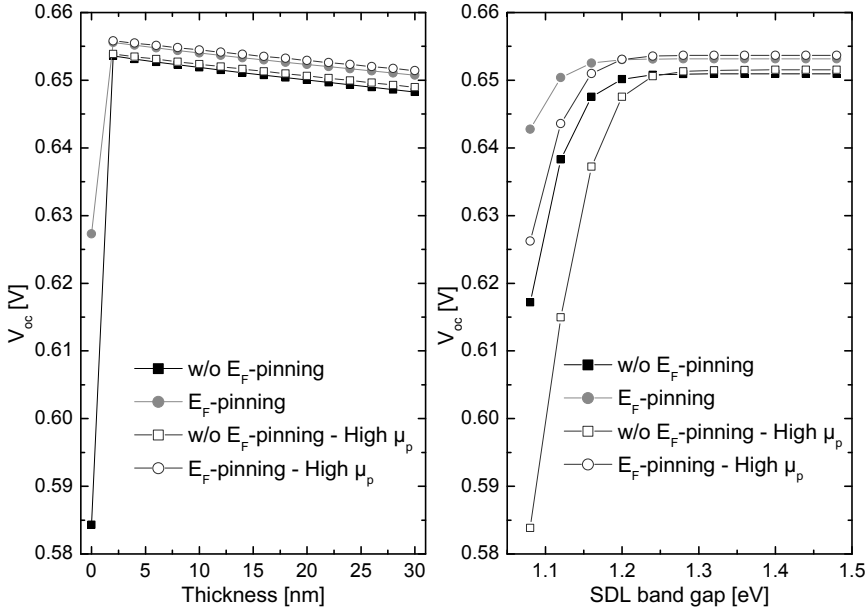


Figure 4.5: Effect on V_{oc} by varying the SDL thickness and band gap in the baseline parameter set. Baseline models with and without E_F -pinning at the absorber-buffer interface are compared. Corresponding models with a hole mobility in the SDL equal to the hole mobility in the CIGS-bulk ($12.5 \text{ cm}^2/\text{Vs}$) are also shown. Simulations were performed at 300 K.

As seen in Figure 4.5.a) a high V_{oc} is maintained also for a very thin defect layer. There is even a slight increase in V_{oc} towards thinner layers. However, when removing the SDL there is a drastic loss in V_{oc} due to the lower absorber band gap at the interface towards the buffer, enabling more recombination. A higher hole mobility has no major effect on the solar cell parameter when assuming an SDL with a band gap of 1.33 eV. By lowering the SDL band gap

towards the surface band gap of the bulk CIGS (1.08 eV) the V_{oc} is reduced. However it is apparent when comparing Figs. 4.5.a) and b) that the V_{oc} values do not reach the level of the model missing SDL. By raising the hole mobility to the bulk value though, the V_{oc} values of both models fall to the values obtained without SDL.

4.2 Electrical Characteristics of CIGS-Cells with Alternative Buffer Layers

We have also studied CIGS-devices with alternative buffer layers. In the following sections some characteristics of ALD- $\text{Zn}_{1-x}\text{Mg}_x\text{O}$ are discussed and results of modelling cells with such buffer layers are presented. In section 4.3.3 results of simulations including ALD- $\text{Zn}(\text{O},\text{S})$ buffer layers are displayed in connection with the discussion on effects of varying the CIGS absorber layer thickness.

4.2.1 Measurements on $\text{Zn}_{1-x}\text{Mg}_x\text{O}$ Thin-Films

We prepared nine ALD- $\text{Zn}_{1-x}\text{Mg}_x\text{O}$ thin-film samples of different thicknesses and compositions in Paper III. Table 4.2 gives an overview of these samples. Thicknesses were obtained from profilometer measurements. The Mg-content was determined indirectly by optically measuring the band gap. These band gap values were then related to compositional data obtained previously from XRF and x-ray reflectivity (XRR) measurements [72].

We found that the resistivity of these films as measured in darkness decreases with illumination time. This is demonstrated in Figure 4.6.a) where the films are illuminated with the UV-lamp. The effect is stronger for thinner films with higher Mg-content. The resistivity stays on a lower level for weeks when films are stored in darkness at RT as shown in Paper III. At higher temperatures relaxation is faster. Figure 4.6.b) displays the effect of annealing the films at 370 K. In the next section a background to this type of behaviour, known as persistent photo conductivity (PPC), is given.

Hall measurements were performed in darkness on $1\text{ cm}^2 \times 1\text{ cm}^2$ sample pieces using the method described in Section 2.4. Measured charge carrier densities and mobilities obtained before and after light-soaking as well as after relaxation are shown in Figures 4.7.a) and b). Each sample was measured a number of times in order to check the reproducibility of the obtained values. Each point in the figure corresponds to one measurement. All samples were found to be of n-type conduction. We found that the increase in conductivity consists of increases both in the carrier density and the mobility.

Wavelength dependent LS of $\text{Zn}_{1-x}\text{Mg}_x\text{O}$ thin-films was also presented in Paper III. It was found that 15 min of blue LED-illumination induced PPC in

Table 4.2: The thicknesses, compositions (x) and bandgaps (E_g) of the different films. Using the bandgap values, compositions were extrapolated from existing compositional measurement data. As explained in Section 1.2.2 the process denoted $\text{Zn}_{1-x}\text{Mg}_x\text{O}$ (1:9) is made up of cycles where a Mg-precursor pulse is followed by nine Zn-precursor pulses

Sample name	Material	Thickness [μm]	E_g [eV]	x
A	ZnO	0.20	3.29	0
B	ZnO	0.43	3.29	0
C	ZnO	0.93	3.29	0
D	$\text{Zn}_{1-x}\text{Mg}_x\text{O}$ (1:9)	0.20	3.47	0.12
E	$\text{Zn}_{1-x}\text{Mg}_x\text{O}$ (1:9)	0.40	3.47	0.12
F	$\text{Zn}_{1-x}\text{Mg}_x\text{O}$ (1:9)	0.84	3.47	0.12
G	$\text{Zn}_{1-x}\text{Mg}_x\text{O}$ (1:6)	0.19	3.57	0.17
H	$\text{Zn}_{1-x}\text{Mg}_x\text{O}$ (1:6)	0.40	3.57	0.17
I	$\text{Zn}_{1-x}\text{Mg}_x\text{O}$ (1:6)	0.82	3.57	0.17

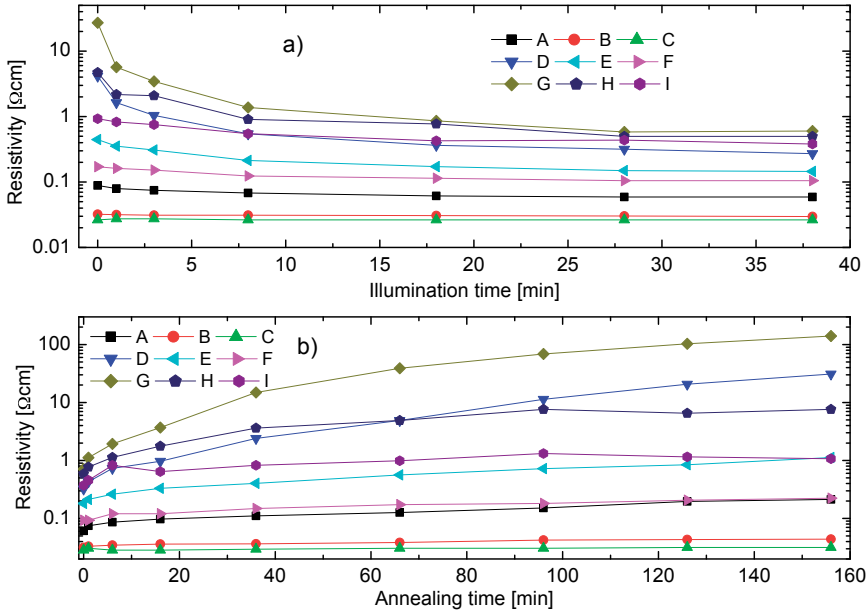


Figure 4.6: Evolution of resistivity during UV-illumination in a) and during annealing at 370 K in b). Measurements are performed using a four-point probe.

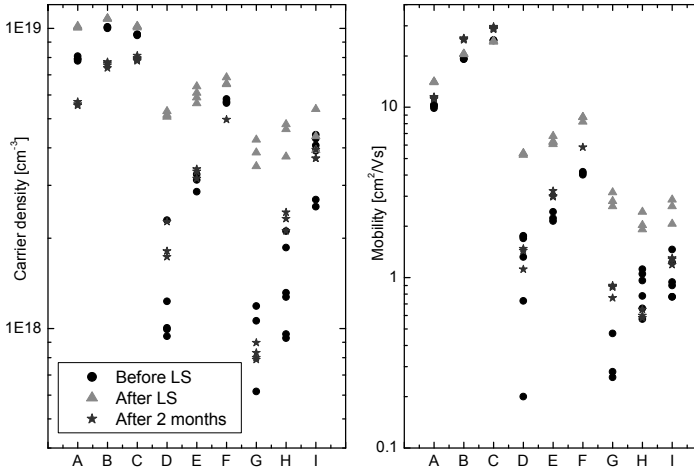


Figure 4.7: Measured carrier densities and mobilities of the different $\text{Zn}_{1-x}\text{Mg}_x\text{O}$ samples. Measurements conducted in darkness before and after 30min UV-illumination as well as after two months of dark storage. Each point corresponds to one measurement.

the Mg-containing films. Red and green LED-illumination did not affect the films significantly.

4.2.2 Persistent Photoconductivity

Photoconductivity is the excess conductivity induced in semiconducting materials due to light-generated charge carriers. Photoconductivity typically decays within fractions of a second following the end of illumination. PPC on the other hand stays for much longer times. Unlike ordinary photoconductivity which depends on light intensity alone, the level of PPC is a function of both the light intensity and the irradiation time [28, 55].

Two models are most commonly used to explain the existence of PPC in various semiconductors. One is the model of local potential fluctuations due to compositional variations that was proposed by Sheinkman and Shik [68]. These fluctuations separate electrons in the conduction band and holes in the valence band spatially and thereby function as barriers to recombination of charge carriers excited over the bandgap. The existence of PPC in for example ZnCdSe and CdSSe single-crystalline alloys has been attributed to such random fluctuations [13, 27].

Lang and coworkers explained PPC in AlGaAs:Te by the existence of a type of defects called DX centres [34, 35]. The mechanism behind n-type PPC would in this model be that electrons residing in deep levels at defect centres get excited by light absorption. The excitations cause large lattice relaxations

around the DX centres which leads to rearrangement of the defect energy levels and that free electrons are released into the conduction band. This leads to the persistently higher n-doping since there is a thermal barrier inhibiting relaxation of the defect centre into the original state.

PPC is most prevalent at temperatures much below room temperature but in for example ZnCdTe thin films PPC with long relaxation times was observed at room temperature. Also here the effect was attributed to the DX centre model [14]. Both the mentioned sources of PPC might be present in a material at the same time, even if one of them is being dominant.

A number of authors have studied PPC in ZnO and related materials. Polyakov et. al. observed it both in undoped hydrothermally grown bulk ZnO and in phosphorous-doped (Zn,Mg)O thin films grown by pulsed laser deposition [51, 53]. In both materials they attribute PPC to localized deep states induced by DX centers. In contrast, PPC in nitrogen-doped single-crystalline ZnO grown by molecular beam epitaxy (MBE) was explained by local potential fluctuations [52]. First-principles electronic structure calculations performed by Lany and Zunger give at hand that DX centres due to oxygen vacancies could give rise to PPC in ZnO [36]. Quite recently, a new model was introduced to explain n-type PPC in p-type ZnO:N and ZnO:P crystals grown by MBE [11]. There the persistent increase of conductivity following illumination was ascribed to electrons confined in a channel at the surface, caused by surface donor trap-states, and thereby becoming spatially separated from the holes dominating the bulk.

4.2.3 Modelling of CIGS-devices with $\text{Zn}_{1-x}\text{Mg}_x\text{O}$ buffer layers

We found in Paper II that for many $\text{Zn}_{1-x}\text{Mg}_x\text{O}$ compositions, cells with such buffer layers show significant increases in efficiency with illumination time. For cells with ZnO buffer layers, light-soaking mainly causes an increase in V_{oc} while for Mg-rich buffers the major effect is an improvement in FF. This behavior is shown in Figure 4.8. For very Mg-rich buffers, deposited with the 1:4 process, there is even a significant J_{sc} loss in the relaxed state.

Devices with pure ZnO buffer layers and with Mg-containing buffers deposited in the ALD-reactor using the 1:6 process, were selected for modelling in Paper VI. Both types of cells show prominent light-soaking behaviour and are therefore suitable for studying such effects. Additionally the (Zn,Mg)O 1:6 process was found to give single-phase wurtzite films while films having higher Mg-content were two-phase [72]. Electrical simulations in one dimension would probably not be suitable for cells with buffer layers consisting of two phases. In the work of Törndahl et. al. the 1:6 process resulted in $\text{Zn}_{1-x}\text{Mg}_x\text{O}$ films with $x=0.19$. As displayed in Table 4.2 we found in Paper III that the corresponding process gave films with $x=0.17$, which is very close to the previously measured value. It is worth to note that the error in x is about

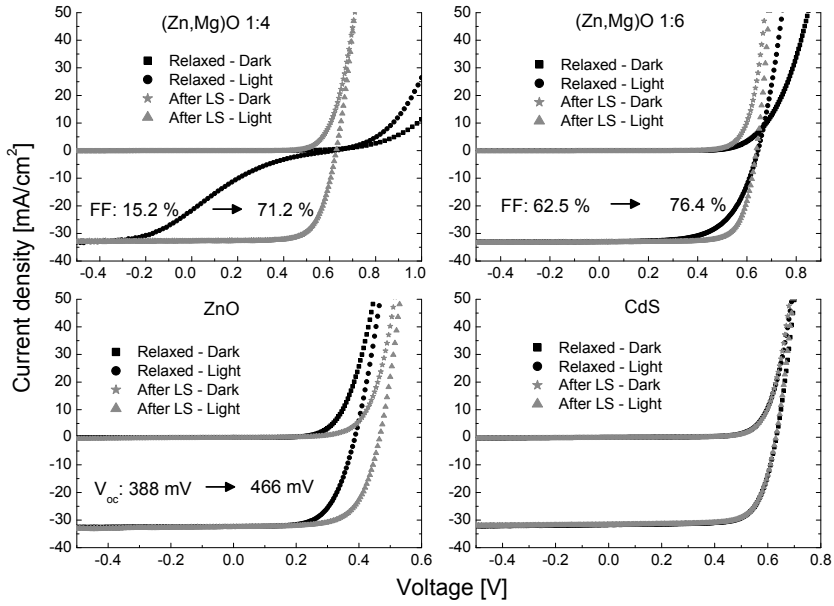


Figure 4.8: JV measurements of cells with $Zn_{1-x}Mg_xO$ buffers of different compositions. Curves in the relaxed state and after light-soaking are shown. Shown for comparison are data for a cell with a CdS buffer layer.

10% [72]. From here on I will denote the 1:6 buffer layers as $\text{Zn}_{0.83}\text{Mg}_{0.17}\text{O}$ buffers.

Electrical parameters of the $\text{Zn}_{1-x}\text{Mg}_x\text{O}$ buffer layers were based on the ZnO parameters in the baseline model alongside with measurement data. The parameters used in SCAPS are displayed in Table 4.3. We determined the Mg-content, absorption data and band gap of the buffer layers in Papers II and VI indirectly by studying thin films deposited on glass using the same ALD-process. Mobility and doping values were based on the Hall measurements presented in Paper III and Section 4.2.1. CBOs between the absorber and the different buffers were estimated based on previous VBO-measurements in our group, conducted on devices with pure ALD-ZnO as buffer layer [48, 50]. How the CBO-values used in simulations are determined is further discussed in Paper VI. When developing our models in Paper VI we also take into account that the JVT-measurements in Paper II indicate interface recombination limited V_{oc} for cells with ZnO buffer layers. When the Mg-content in the buffer increases, interface recombination is reduced.

To reproduce the development of the JV-curves with light-soaking some additions to the models were necessary. Simulations in the relaxed state using the $\text{Zn}_{0.83}\text{Mg}_{0.17}\text{O}$ cell model of Table 4.3 do not give as low FF as in measurements. Furthermore do simulations with the ZnO model result in much higher V_{oc} as well as much smaller light-soaking effect as compared to measurements.

A number of models that could explain the light-soaking behavior were introduced in Paper VI. A common trait of all these models, outlined in Table 4.4, is a high density of acceptors somewhere in the buffer region. The function of these excess acceptors is to introduce negative charge, that in the relaxed state works as barriers to light-generated electrons arriving from the CIGS absorber. This is demonstrated in Figure 4.9 where band diagrams obtained at a forward bias of 0.5 V for models A-D, are plotted. In each model the barrier is lowered in the light-soaked state because of the increased buffer doping. The reason to include absorber-buffer interface acceptors in the ZnO models is to make this interface less inverted and thereby increase interface recombination at forward bias and reduce V_{oc} . In the light-soaked state the interface becomes more inverted as displayed in the band diagrams of Figure 4.10. The diagrams are calculated at 0.35 V. More detailed descriptions of the various models can be found in Paper VI.

4.2.4 Light-Soaking Behaviour of $\text{Zn}_{1-x}\text{Mg}_x\text{O}$ -Cells and Thin-Films

In Paper VI the conductivity development in a $\text{Zn}_{0.83}\text{Mg}_{0.17}\text{O}$ thin film with UV-illumination time (Figure 4.11.a) was studied and related to simulations. Figure 4.11.b) displays how the FF is dependent on $\text{Zn}_{0.83}\text{Mg}_{0.17}\text{O}$ doping in simulations with the models introduced in Section 4.2.3. The behaviour is

Table 4.3: *This table displays the parameters used in most of this work when modelling ALD-Zn_{1-x}Mg_xO buffer layers. First and second values of the mobilities and doping densities are for the relaxed and light-soaked states, respectively.*

Layer Properties		
	ALD-ZnO	ALD-Zn_{0.83}Mg_{0.17}O
Thickness [μm]	0.2	0.19
E_g [eV]	3.30	3.57
ϵ_r	9	9
N_C [cm^{-3}]	3×10^{18}	3×10^{18}
N_V [cm^{-3}]	1.7×10^{19}	1.7×10^{19}
v_{th}^n [cm/s]	2.4×10^7	2.4×10^7
v_{th}^p [cm/s]	1.3×10^7	1.3×10^7
μ_n [cm^2/Vs]	11/14	0.9/3.0
μ_p [cm^2/Vs]	3.4/4.3	0.3/0.9
Doping [cm^{-3}]	$6 \times 10^{18}/10^{19}$ (d)	$8 \times 10^{17}/4 \times 10^{18}$ (d)
Bulk Defect Properties		
N [cm^{-3}]	10^{16} (A)	10^{16} (A)
σ_n [cm^2]	10^{-15}	10^{-15}
σ_p [cm^2]	5×10^{-13}	5×10^{-13}

Table 4.4: *An overview of the different models developed to reproduce measurement data in SCAPS. It is indicated which of the models that include SDL. In the case of model C the same result is obtained from simulations with and without SDL. For each model the value of the CBO between the absorber and buffer layers is shown. Additionally, it is displayed where the excess acceptors specific for each model, are positioned. More details on these device models were presented in Paper VI.*

Buffer Layer	Model	SDL?	CBO [eV]	Excess Acceptor Placement
Zn _{0.83} Mg _{0.17} O	A	Yes	0	Abs./Buffer Int.
Zn _{0.83} Mg _{0.17} O	B	Yes	0	SDL
Zn _{0.83} Mg _{0.17} O	C	Yes+No	0	Buffer/Window Int.
Zn _{0.83} Mg _{0.17} O	D	No	0.39	Abs./Buffer Int.
ZnO	E	Yes	-0.33	Abs./Buffer Int.
ZnO	F	No	-0.08	Abs./Buffer Int.

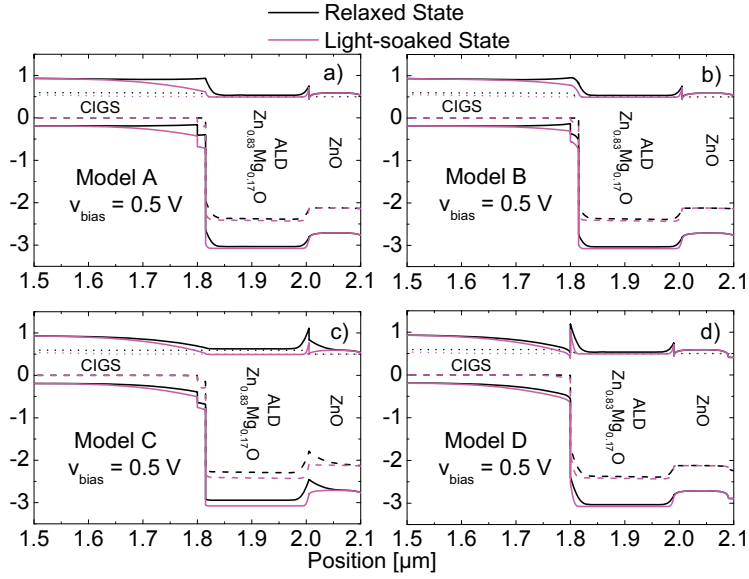


Figure 4.9: Here band diagrams in the relaxed and light-soaked states are shown for the four models of the cells with $\text{Zn}_{0.83}\text{Mg}_{0.17}\text{O}$ buffer layers. Focus is on the buffer region. To emphasize the barriers to the light current, diagrams recorded at a forward bias of 0.5 V are shown. An overview of the models is given in Table 4.4. Dotted and dashed lines indicate electron and hole quasi Fermi levels, respectively.

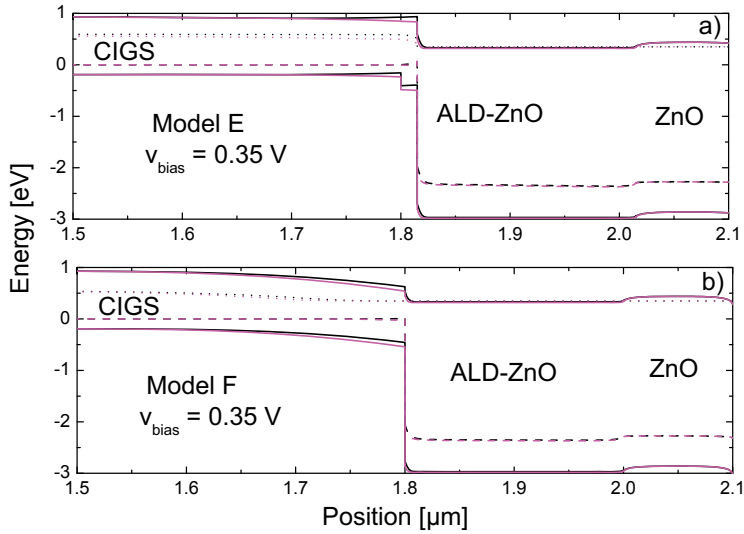


Figure 4.10: Band diagrams showing the buffer region of the two ZnO-cell models in the relaxed and light-soaked states. Also here, diagrams obtained at forward bias are shown. An overview of the models is given in Table 4.4. Dotted and dashed lines indicate electron and hole quasi Fermi levels, respectively.

similar for all device models, with a rapid initial increase in FF followed by a saturation. Doping limits are the values for the relaxed and light-soaked states presented in Table 4.3. It is visible in a) that the conductivity increase in the film is roughly linear with time in the measured interval. If it is assumed that the linearity in conductivity during PPC buildup corresponds to a roughly linear increase in $\text{Zn}_{0.83}\text{Mg}_{0.17}\text{O}$ doping it can be deduced that the FF-dependence on doping in b) should be similar to the evolution of the FF with illumination time. This is also the case as demonstrated in Figure 4.11.c) where the light-soaking behaviour of two cells with $\text{Zn}_{0.83}\text{Mg}_{0.17}\text{O}$ buffer is shown. The distance to the UV-source is the same in a) and c). This similarity between measurements and simulations strengthens the hypothesis that PPC in the $\text{Zn}_{1-x}\text{Mg}_x\text{O}$ layers is important for the FF improvement seen during illumination of cells.

Recently I have also studied the effects of illuminating the $\text{Zn}_{1-x}\text{Mg}_x\text{O}$ devices with LEDs. To avoid blue light-soaking during measurements, JV curves were recorded with a red filter having a cut-off frequency of 580 nm, in front of the halogen lamp. Analogous to what was found for the conductivity of thin films I found a significant increase in FF of the cells with Mg-rich buffer layers induced by 15 min of blue illumination. Red and green light decreases the FF of these cells, significantly. This is in contrast with the corresponding thin films for which red and green illumination gave no significant resistivity changes.

Curves from Paper VI showing JV simulation results obtained at RT using the models presented in Table 4.4, are displayed in Figure 4.12. In the figure JV curves obtained in the relaxed and light-soaked states are compared with corresponding measurements. From Figures 4.4.a) and b) it can be concluded that models A, B and D all give rather good fits to measurements on $\text{Zn}_{0.83}\text{Mg}_{0.17}\text{O}$ devices. The best correspondence is given by model D. For the ZnO devices both models E and F give good results as displayed in Figures 4.4.c) and d). In Paper VI also RT dark curves and low-temperature light curves were studied. At 200 K, models B and F give the JV-curves most similar to measurements for the $\text{Zn}_{0.83}\text{Mg}_{0.17}\text{O}$ and ZnO devices, respectively. The light-dark JV cross-over of the $\text{Zn}_{0.83}\text{Mg}_{0.17}\text{O}$ -samples at RT was reproducible by introducing a high density of compensating acceptors into model D. These acceptors must have very unequal capture cross-sections for electrons and holes. This model also reproduces the other measured JV-curves relatively well. The effective doping in this model is however slightly lower than measured by the Hall effect.

It could be concluded from Paper VI that there are a number of models that could explain the light-soaking behaviour of devices with $\text{Zn}_{1-x}\text{Mg}_x\text{O}$ buffer layers using the measured doping, carrier mobility and absorber-buffer VBO values. All of these models include acceptors somewhere in the buffer region. The existence of a SDL is not necessary to reproduce measurement data.

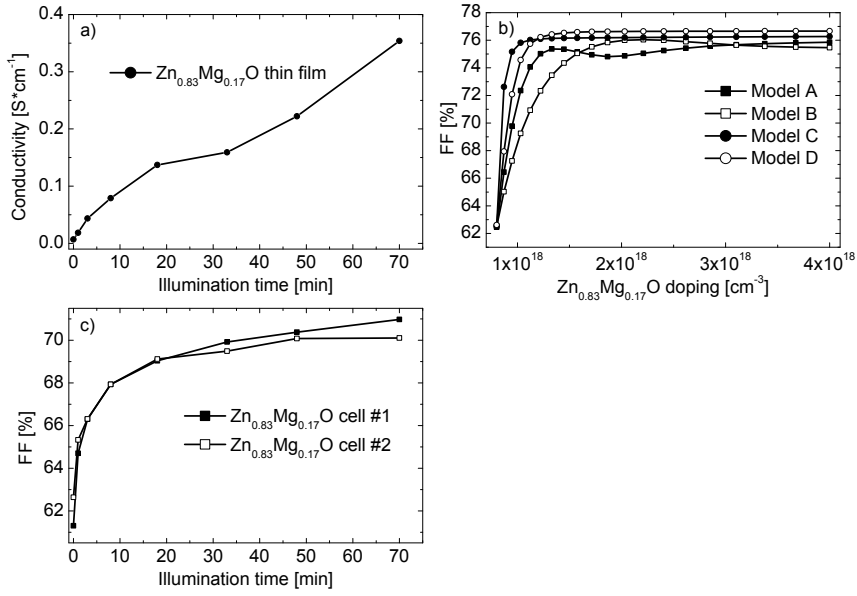


Figure 4.11: In a) development of the conductivity of a $\text{Zn}_{0.83}\text{Mg}_{0.17}\text{O}$ thin film during illumination with UV-light is shown. In b) the effect on the FF of varying the buffer doping in the different $\text{Zn}_{0.83}\text{Mg}_{0.17}\text{O}$ device models is demonstrated. Doping is varied within the range based on measurements, presented in Table 4.3. Measured UV-light-soaking behaviour of two different $\text{Zn}_{0.83}\text{Mg}_{0.17}\text{O}$ cells is shown in c)

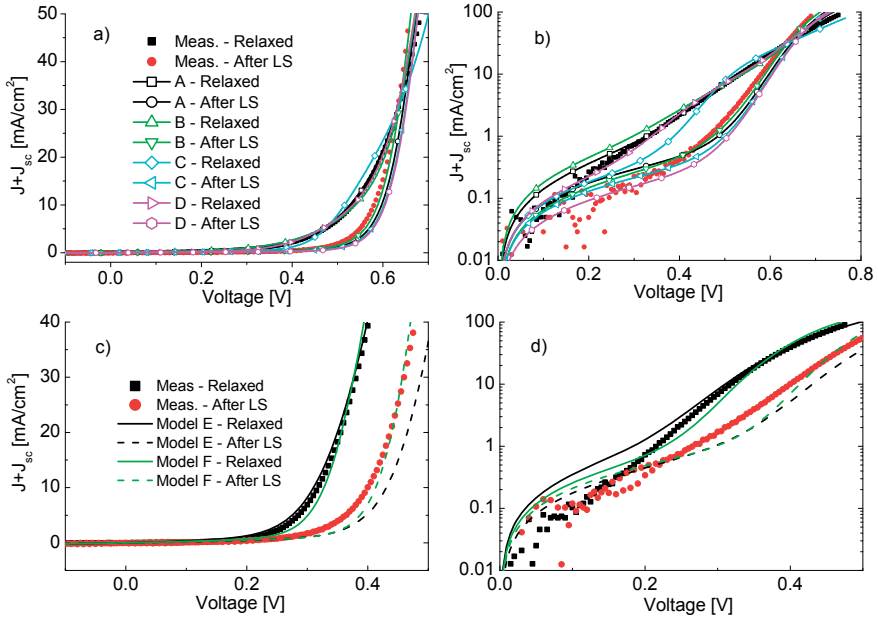


Figure 4.12: Light JV-curves obtained from simulations at RT using the different $\text{Zn}_{0.83}\text{Mg}_{0.17}\text{O}$ (Figs. a and b) and ZnO (Figs. c and d) device models of Table 4.4, in relaxed and light-soaked states. Simulations are compared with RT measurements. Current data is shifted with J_{sc} . In a) and c) linear JV-curves are displayed while in b) and d) semi-logarithmic curves are shown.

An important material parameter in modelling is the CBO between the absorber and the buffer layers. Taken the measured VBO as a fixed parameter the presence of the SDL affects the CBO used in simulations. Very positive CBO-values for Mg-rich buffer layers and very negative CBO-values for pure ZnO buffers facilitate modelling of light-soaking in the corresponding devices. The dark-light cross-over of cells with $\text{Zn}_{0.83}\text{Mg}_{0.17}\text{O}$ buffers can be reproduced by assuming a high CBO and a somewhat lower effective doping than what was measured in thin films.

I have also been able to model the light-soaking behaviour of the $\text{Zn}_{1-x}\text{Mg}_x\text{O}$ cells in AFORS-HET by changing the models of Paper VI slightly. These changes mainly consisted in lowering mid-gap interface defects in comparison to the SCAPS models to keep the V_{oc} on par with measurements. It is unclear why the structures are more sensitive to interface recombination in AFORS-HET than in SCAPS.

4.2.5 Modelling $\text{ZnO}_{1-y}\text{S}_y$ Buffer Layers

In Paper VII cells with varying absorber thickness and $\text{ZnO}_{1-y}\text{S}_y$ buffer layers were modelled. This type of ALD buffer layer has a sulfur rich surface towards the CIGS layer as found experimentally in the work by Platzer-Björkman et al. [47]. In simulations the $\text{ZnO}_{1-y}\text{S}_y$ buffer is therefore divided into a high band gap (3.0 eV) sulfur-rich interface layer ($y = 0.7$) closest to the absorber and a less sulfur containing ($y = 0.3$) thicker layer with lower band gap (2.7 eV), towards the undoped ZnO layer. Zn(O,S) band gap values and conduction band offsets between the Zn(O,S) layers as well as towards the CIGS layer are taken from [47]. The Zn(O,S) doping level was selected by fitting the trends in measured JV parameters and is similar to what was found by Hall measurements on Zn(Mg,O) buffers in Paper III. Parameter values are tabled in Paper VII.

4.3 Results of Absorber Layer Modifications

In this part of the thesis I will mainly focus on the effects of changes in the absorber layer as studied in Papers I, V and VII. However, in the work related to Papers I and VII, in addition to standard cells with CdS buffers, devices having alternative buffer layers were processed. Therefore buffer depending properties must also be considered in the following sections.

4.3.1 Characteristics of Cells with CGS Absorbers

Devices with pure CGS absorber layers were processed and characterized in Paper I. CGS cells with alternative buffer layers from the ALD reactor were compared with cells having chemical bath deposition (CBD)-CdS buffers. A

number of different (Zn,Mg)O and Zn(O,S) buffer compositions were studied. We found that the (Zn,Mg)O 1:5 and Zn(O,S) 1:9 processes gave the best cells, for the respective buffer layer types, with a maximum efficiency of 6.2 % and 3.9 %, respectively. My contribution to Paper I was to perform JVT-measurements on sample cells from substrates having CdS, (Zn,Mg)O 1:5 and Zn(O,S) 1:9 buffer layers. JV curves obtained in darkness and under illumination were studied for temperatures between 200 K and 340 K.

For all samples there was a large spread in the activation energies extracted using the three methods presented in Section 2.1.4. For the alternative buffer layers activation energies generally were lower than the band gap of CGS which is between 1.6 eV and 1.7 eV. This is a sign of interface recombination limiting V_{oc} . On the other hand, for CdS cells activation energies were close to the band gap energy when measuring in the relaxed state while there was a tendency towards lower activation energies after light-soaking. Fits of the ideality factors of devices with CdS buffers to the two models of temperature-dependence, mentioned in Section 2.1.4, indicated recombination in the depletion region being dominant.

4.3.2 Influence of In-Rich Surface Layers

In the work of Paper V, CIGS layers were deposited using the three-stage process. In addition to reference devices made with the standard process we also fabricated samples for which the CIGS-evaporation was ended with a stage where only In and no Ga was evaporated. The length of the final step was varied between the samples so that cells with CIS top layers having nominal thicknesses of 20 nm, 50 nm and 100 nm were produced. On all CIGS films CdS buffer layers were deposited. The result of the CIGS-process modifications was a lowering of the band gap in the region of the absorber closest to the CdS. Light JV-parameters resulting from device measurements are displayed in Table 4.5.

My contribution to Paper V was to model the devices in SCAPS and to perform JV and CV measurements on two of the samples at various temperatures. Since a considerably different CIGS evaporation process was used for the devices of this paper a number of modifications to the baseline model were necessary in order to be able to reproduce JV and QE curves of the reference sample. One major difference was in the CIGS compositional grading. The various Ga/III compositional gradings utilized in the simulations of this thesis are exhibited in Figure 4.13. Other changes to the baseline model are discussed in the paper.

Proceeding from the reference sample to the devices with deposited CIS top layers, the only modification of the model was to introduce the compositional profiles with linearly decreasing Ga/III-ratios towards the CdS buffer. Profiles are displayed in Figure 4.13.b). Based on the SIMS measurements the extent of the linear regimes are chosen as twice the nominal thicknesses of the

deposited CIS. Solar cell parameters obtained from simulations are presented in Table 4.5.

Except reproducing the processed devices attempts were made to predict more extreme situations with thicker deposited CIS layers. These estimated compositional profiles are also shown in Figure 4.13.b). We assumed that the slope of the linear grading is the same as for the 100nm devices. It can be noted that the lower absorber surface band gap of the modified samples also implicates that the CBO towards the CdS gets higher. This is accounted for in the simulations.

When building the models we took into consideration that bulk recombination was found to be the dominant recombination path for both the reference and the 100nm devices. The apparent doping profiles extracted from CV measurements conducted at temperatures around 150K, were in the range of 10^{15} cm^{-3} to 10^{16} cm^{-3} .

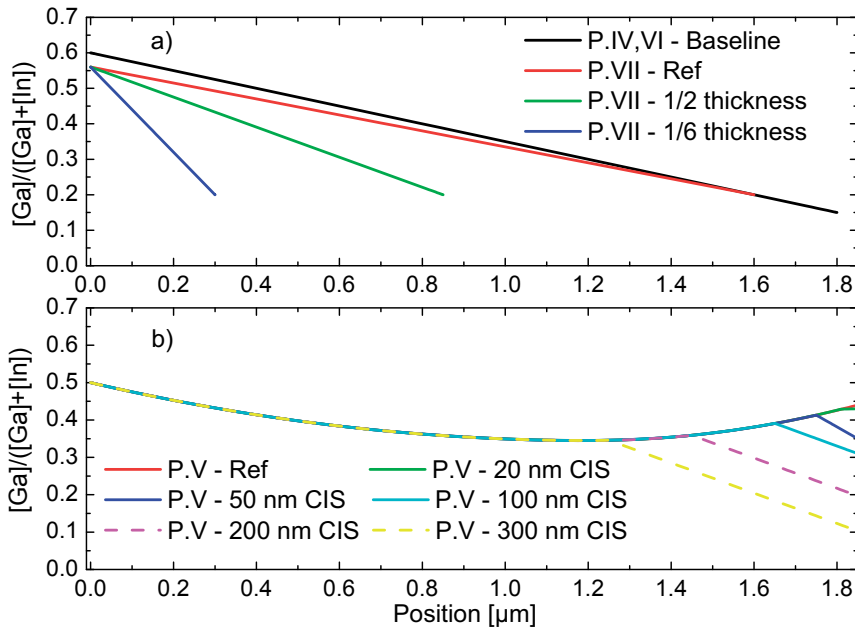


Figure 4.13: Gallium grading profiles used in this thesis for modelling the CIGS absorber layer in SCAPS. From these GGI profiles the band gap variations were calculated. In the legend it is indicated in what papers each profile was used. Dashed lines in b) indicate those profiles designed to predict the behaviour of cells not fabricated, rather than to reproduce the properties of finished devices. Each profile is plotted so that the the origin of the position-axis is placed at the back contact.

As seen in Table 4.5, Figure 4.14 and in Paper V there is a relatively good correspondence between simulated and measured JV and QE curves of the reference cell. There are only minor differences in the JV parameters between

Table 4.5: *Solar cell parameters from measurements and simulations in Paper V.*

	V_{oc} [mV]	J_{sc} [mA cm ⁻²]	FF [%]	η [%]
Measurements				
Reference	685	31.4	75.2	16.2
20 nm CIS	687	31.5	76.8	16.6
50 nm CIS	674	32.0	75.4	16.3
100 nm CIS	679	31.8	75.0	16.2
Simulations				
Reference	689	31.7	77.4	16.9
20 nm CIS	688	31.7	77.4	16.9
50 nm CIS	688	31.7	77.2	16.8
100 nm CIS	687	31.8	77.2	16.9
200 nm CIS	673	32.7	77.7	17.1
300 nm CIS	643	34.1	77.1	16.9

the reference and the sample cells having an intentionally lower front surface band gap. There is a small trend of decreasing V_{oc} with increasing thickness of the deposited CIS layer. Such a trend, though even smaller, is also seen in the corresponding simulations and is due to a slight increase in interface recombination. This trend is however more pronounced for the models of devices with thicker CIS layers of 200 nm and 300 nm nominally. In these cases significantly higher J_{sc} values are obtained. This is caused by the low surface band gaps, which now have become lower than the minimum notch of the reference model (see Fig. 4.13). The effect is obvious in Figure 4.14 where the QE curves of the 200 nm and 300 nm models extend further into long wavelengths than the other simulated curves.

We compared our cells with NRELs record CIGS device with an efficiency of 20.0%, that was presented by Repins et. al. [59] and tried to approach their efficiency in simulations by modifying our model. This efficiency was possible to reach by reducing the CIGS bulk and CIGS-CdS interface defect densities and additionally reducing the front contact reflection. The largest improvement was due to the reduction of defects in the CIGS layer.

From this work we concluded that no significant improvement of the cell efficiency, by depositing a thin CIS layer at the end of the CIGS deposition process, was found. The same is seen in simulations. However if this Ga-poor surface layer would improve lattice matching and thereby reduce the interface defect density there can be a small positive effect. A thick CIS layer deposited on top of the CIGS would lead to the beneficial effect of an increased J_{sc} . We

also concluded that the absorber diffusion length is the main factor limiting the performance of our three-stage CIGS devices with CdS buffer layers.

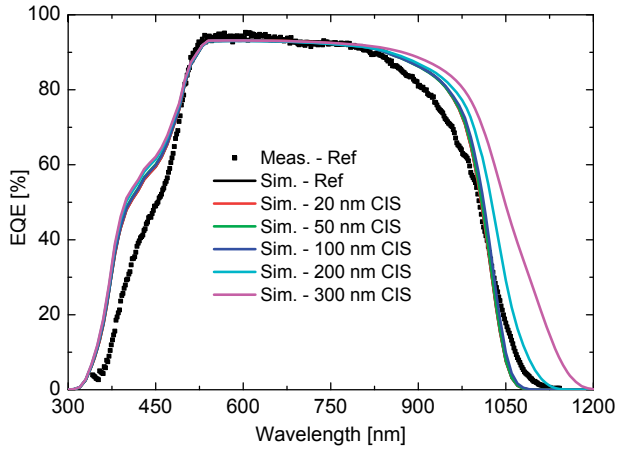


Figure 4.14: QE curves resulting from simulations. For comparison the measured QE curve of the reference sample is displayed.

4.3.3 Effects of Varying the CIGS-Absorber Thickness

Samples fabricated in Paper VII are presented in Table 4.6. This table shows the CIGS absorber thickness of each sample and the average Ga/III and Cu/III ratios measured by XRF.

Table 4.6: Solar cell samples studied in Paper VII.

Sample	Buffer layer	CIGS thickness (Profilometer) [μm]	Ga/III (XRF) [%]	Cu/III (XRF) [%]
ZnOSx1	$\text{ZnO}_{1-y}\text{S}_y$	1.5-1.7	45	92
CdSx1	CdS	1.5-1.7	45	92
ZnOSx1/2	$\text{ZnO}_{1-y}\text{S}_y$	0.8-0.9	46	90
CdSx1/2	CdS	0.8-0.9	46	90
ZnOSx1/6	$\text{ZnO}_{1-y}\text{S}_y$	0.3	46	87
CdSx1/6	CdS	0.3	46	87

In Table 4.7 the measured JV parameters for the different samples are shown alongside results from simulations. The IQE curves are compared in Figure 4.15.

Table 4.7: In this table solar cell JV parameters from measurements and simulations are shown. Measured values on the left are medians for each sample. Simulated J_{sc} values are compared with values calculated from measured IQE curves shown within parentheses. Also the recombination path limiting V_{oc} in simulations is indicated. Int. and BC are abbreviations for interface and back contact recombination, respectively. In the ZnOSx1/2 sample two recombination paths are of similar importance for V_{oc} .

Sample	Measurements				Simulations			
	V_{oc} [mV]	J_{sc} [mA cm ⁻²]	FF [%]	η [%]	V_{oc} [mV]	J_{sc} (IQE) [mA cm ⁻²]	FF [%]	Recombination [-]
ZnOSx1	668	32.8	71.9	16.2	693	38.1 (36.6)	79.2	CIGS
CdSx1	679	31.1	74.6	15.8	708	36.1 (34.3)	79.3	CIGS
ZnOSx1/2	685	30.1	71.9	14.8	701	35.5 (33.4)	79.6	Int./CIGS
CdSx1/2	681	26.7	75.7	13.8	728	33.5 (30.0)	79.2	CIGS
ZnOSx1/6	644	20.8	69.3	9.6	696	26.7 (23.4)	79.1	Int.
CdSx1/6	666	17.1	73.6	8.4	723	25.0 (19.2)	79.3	BC

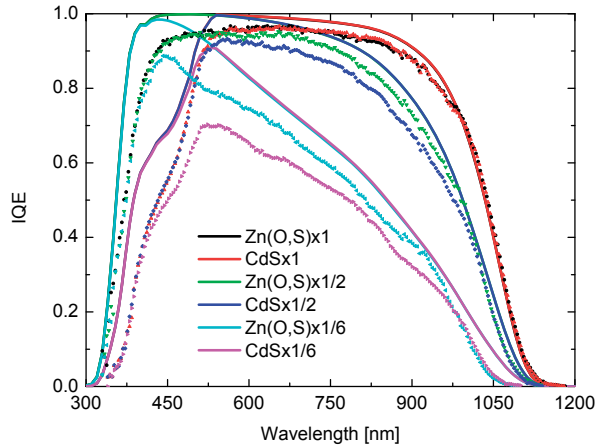


Figure 4.15: Comparison of measured IQE curves (scattered data) and simulation results (lines) for the six samples. Each scatter plot is an average of measurements on four cells.

As seen in Table 4.7 and Figure 4.15 trends in measured JV and QE curves could relatively well be reproduced in simulations. The direction of changes as a function of thickness are in general similar to measurements. Recombination in the CIGS layer is reduced with thickness while back contact recombination gains in magnitude. This results in that the samples with absorbers of intermediate thickness display the highest V_{oc} . The highest efficiencies are found for devices of standard thickness, due to the high J_{sc} . Cells of standard thickness have comparable efficiency regardless of buffer layer. Thinner devices with $\text{ZnO}_{1-y}\text{S}_y$ buffer layers are however significantly more efficient than their CdS references. This better performance is an effect of a higher QE level across the entire sensitive wavelength range. The considerable QE difference below 500 nm is due to less UV and blue light absorption in $\text{ZnO}_{1-y}\text{S}_y$, a result of the higher band gap.

V_{oc} of the thinnest devices with CdS is limited by recombination at the back contact. For the thin $\text{ZnO}_{1-y}\text{S}_y$ cells interface recombination is also important. This is in accordance with JVT measurements on thin $\text{ZnO}_{1-y}\text{S}_y$ samples. In the standard devices recombination in the CIGS layer is dominant. The other recombination paths could however become a problem if the CIGS material would be sufficiently improved.

A narrower depletion width was found in CV measurements on the thinner CdS samples in comparison to the samples with $\text{ZnO}_{1-y}\text{S}_y$ buffer layers. However since no voltage dependent current collection was found, we find it difficult to explain the difference in QE above 500 nm by this observation. To understand this feature more advanced optical as well as structural characterization of the material seems necessary. Optical and electrical modelling in more than one dimension might also be fruitful.

4.4 A Discussion on Metastabilities

The question whether metastabilities in CIGS solar cells have their root in the buffer or the absorber layer is a much debated one. The answer probably depends on what metastability you consider and it is likely often so that both of the layers as well as the interface in between have an influence on the observed behaviour.

The work of this thesis indicates that PPC in the buffer layer could be the root of the FF and V_{oc} blue lightsoaking behaviour of devices with (Zn,Mg)O buffer layers. However it seems like acceptor defects close to the CIGS surface or at the CIGS/(Zn,Mg)O interface also are crucial to explain the magnitude of the effect. PPC in the (Zn,Mg)O thin films is induced by the sub band gap light of a blue LED. This could mean that light is absorbed at a DX centre type defect associated with oxygen vacancies, as was suggested for ZnO in [36]. A high thermal barrier to lattice relaxation would explain the long relaxation times at room temperature.

Red and infrared light has previously been seen to induce metastable effects in the JV properties of cells with CdS buffer layers. Both detrimental [23] and beneficial [57, 60] metastable changes have been observed. In [75] it was found that the influence of red light soaking on cells with CdS and Zn(O,S) cells depends on the cells being in short or open circuit conditions. Open circuit light soaking was in general beneficial while short circuit light soaking was detrimental. This metastable behaviour has been attributed to the light induced change of a copper-selenium vacancy complex into an acceptor configuration [37, 75].

In [75] a FF deterioration induced by red light was found for a single (Zn,Mg)O device. The effect was the same in open and short circuit conditions in contrast to in the cells with CdS and Zn(O,S) buffer layers. As mentioned previously in the thesis I also observe a lowering of the FF in (Zn,Mg)O cells induced by red and green illumination. This light soaking was performed under open circuit conditions. Red and green light soaking on thin films does however not change the buffer conductivity significantly. Considering the earlier measurements, the mechanism behind the FF degradation anyway seems to be connected to the specific properties of the CIGS/(Zn,Mg)O heterojunction.

In future work it would be interesting to measure how the capacitance of the (Zn,Mg)O cells changes when illuminating the devices with light of different wavelengths. These type of measurements could give deeper insight into the root of the metastable behaviour [76].

5. Conclusions

In this thesis I have studied some aspects of how cadmium free buffer layers and absorber layer modifications influence CIGS solar cell properties. As tools in this work I have used various characterization methods as well as electrical device modelling. Both finished devices and individual layers have been characterized. Data from measurements have, alongside with literature data, been used as input in the simulations.

The efficiency of CIGS cells with (Zn,Mg)O buffer layers improved with illumination. This behaviour is metastable and relaxation to the low efficiency stable state, takes weeks in darkness at room temperature. For ZnO cells there was mainly an increase in V_{oc} while for devices with Mg-rich buffer layers there was a considerable increase in the FF. By JVT analysis it was found that interface recombination is limiting V_{oc} in cells with ZnO buffer layers. Interface recombination as well as total recombination is reduced when magnesium is introduced into the ZnO. This is due to the positive CBO between (Zn,Mg)O buffers of high magnesium content and CIGS absorbers of normal gallium content .

PPC is induced in (Zn,Mg)O thin films by illumination. This enhanced conductivity also stays for many weeks in room temperature. According to Hall effect measurements this effect is due to an increase in doping as well as in mobility. Electrical device modelling showed that the measured conductivity changes could explain the light soaking behaviour of CIGS solar cells with (Zn,Mg)O buffer layers. To reproduce the observed behaviour in simulations, it was necessary to assume a high density of acceptors in the buffer-absorber interface region.

Simulations and experiments indicate that the deposition of a thin CIS layer at the end of the absorber evaporation does not give any significant positive nor negative impact on the device performance. Our devices with CdS buffer layers are dominated by recombination in the CIGS layer. It can however not be excluded that an significant improvement would exist for cells dominated by interface recombination. Less gallium at the interface possibly gives a better lattice matching towards CdS. This would lower the interface defect density and thereby enhance the V_{oc} significantly, if interface recombination is a limitation.

Variations of the absorber thickness shows that a thinner CIGS layer improves V_{oc} by reducing recombination. The drawback is that the J_{sc} loss is strong enough to lower the efficiency with respect to devices of standard thick-

ness. For thin enough absorber layers also V_{oc} deteriorates. This loss is due to recombination at the back contact, according to simulations. In thin devices with Zn(O,S) buffer layers there is also a problem with interface recombination. This recombination path is overshadowed in cells of standard thickness, by recombination in the CIGS bulk. Thin cells with Zn(O,S) buffer layers anyway outperform CdS cells with the same absorber thickness. The reason for this is a higher QE in the entire sensitive wavelength range.

The primary factor to improve in our cells with CdS buffer layers is the diffusion length in the CIGS layer. With better material properties back contact recombination will eventually become a problem. It is important to avoid Schottky hole barriers at the back contact since these enhance recombination. In devices with Zn(O,S) and probably also (Zn,Mg)O buffer layers, interface recombination would become a V_{oc} limitation. Another reason to be working more on the interface properties of (Zn,Mg)O cells is to get rid of the light soaking behaviour that these devices suffer from.

Sammanfattning på svenska

Solenergi och solceller

Solen är en enorm energikälla. Nästan alla energislag har sitt yttersta ursprung i fusionsprocesserna i solen. Det enda undantaget är geotermisk energi som har sin källa i sönderfall av radioaktiva ämnen i jordens inre. Solinstrålningen på jordytan en klar sommar dag uppgår till 1 kW m^{-2} . Den energi som når jorden varje minut räcker till mänsklighetens totala energikonsumtion flera dagar. Även om en hel del av instrålningen är svårtillgänglig, så som den som sker över hav, så finns det oerhört mycket kvar att ta till vara. Direkt solenergi borde rimligtvis vara en del av vägen till ett samhälle utan fossila bränslen.

Solceller omvandlar ljus direkt till elektricitet. Vanligtvis består dessa av ett n-dopat och ett p-dopat halvledarmaterial. I halvledare så är grundtillståndet vid den absoluta nollpunkten att alla elektroner fyller energitillstånd i det så kallade valensbandet. Ovanför finns det ett spann med energier som är förbjudna, bandgapet. Genom att absorbera ljuspartiklar, fotoner, så kan elektroner förflyttas upp i energi över bandgapet till ledningsbandet som innehåller en mängd tomma tillstånd. En exciterad elektron lämnar efter sig ett tomt tillstånd i valensbandet. En sådant tillstånd kallas hål. Vid temperaturer över den absoluta nollpunkten är en del tillstånd i ledningsbandet upptagna även i mörker. Elektroner kan röra röra sig fritt i ledningsbandet medan hål kan förflytta sig i valensbandet. På detta sätt kan halvledare leda ström om man lägger på en spänning.

Dopning av en halvledare innebär att man introducerar främmande atomer i dess kristallstruktur. När ett material n-dopas så introduceras elektroner i ledningsbandet medan vid p-dopning introduceras hål i valensbandet. Halvledarmaterial kan även vara dopade i sig själva utan någon tillförsel av främmande atomer. Detta beror på defekter i kristallstrukturen, till exempel att atomer saknas på vissa platser. När ett material av p-typ och ett av n-typ förs samman så bildas en pn-diod. Denna har ett inbyggt elektriskt fält vid pn-övergången som i princip är tomt på elektroner och hål. I en solcell utnyttjas detta fält till att skilja ljusgenererade elektroner och hål åt. På detta sätt kan en elektrisk ström genereras i solcellen, vilken kan användas för att driva elektrisk apparatur. Verkningsgraden i en belyst solcell bestäms av kortslutningsströmmen J_{sc} , spänningen i öppen krets V_{oc} och den så kallade fyllnadsfaktorn, FF. Dessa bestämmer ström-spänningskurvans utseende.

I den vanligaste typen av solcell, den kristallina kisel-solcellen, så består både den p-dopade och den n-dopade sidan av kisel. I andra typer av solceller

kan p- och n-sidorna bestå av olika material. Detta är fallet i till exempel tunnfilmssolceller av CdTe och $\text{CuIn}_{1-x}\text{Ga}_x\text{Se}_2$ (CIGS). Just CIGS-solceller är ämnet för denna avhandling.

Tunnfilmssolceller med ljusabsorberande lager av $\text{CuIn}_{1-x}\text{Ga}_x\text{Se}_2$

$\text{CuIn}_{1-x}\text{Ga}_x\text{Se}_2$ (CIGS) är ett, naturligt p-dopat, halvledarmaterial, bestående av koppar, indium, gallium och selen. Detta material har mycket bra ljusabsorberande egenskaper. Det krävs inte ens $2\mu\text{m}$ CIGS för att i princip absorbera allt inkommande ljus som har högre energi än dess bandgap. Som jämförelse måste kristallina kisel-solceller vara $100\mu\text{m}$ till $200\mu\text{m}$ tjocka. Denna materialbesparing är en fördel hos tunnfilmssolceller och möjliggör även tillverkning på flexibla substrat. Verkningsgraden hos CIGS-solceller är högre än för andra vanliga typer av tunnfilmssolceller så som CdTe och amorft kisel.

I denna avhandling så tillverkas CIGS skikten genom förångning av metalliska källor. CIGS-skiktet deponeras ovanpå en baksideskontakt av molybden som i sin tur ligger på ett glassubstrat. CIGS-ytan beläggs med ett tunnt så kallat buffertlager, vilket är av n-typ, och ska ge ett gränsskikt med gynnsamma egenskaper. Detta skikt består i vanliga fall av CdS men detta material har flera nackdelar. Dels förloras rätt mycket ljus på grund av absorption i CdS och dels är kadmium farligt för hälsa och miljö. I denna avhandling har vi studerat celler med $(\text{Zn,Mg})\text{O}$ och $\text{Zn}(\text{O,S})$ som är potentiella ersättningsmaterial med högre bandgap än CdS. Avslutningsvis deponeras ett tunt odopat samt ett tjockare högdopat ZnO-lager. Båda lager är av n-typ och utgör tillsammans en genomskinlig och ledande framsideskontakt.

Bandgapet i CIGS varierar beroende på hur stor del gallium som ingår i förhållande till indium. Ju mer gallium som ingår desto högre bandgap. Det finns ett optimalt bandgap för solcellsändamål som ligger emellan extrempunkterna. Detta beror på att ett högt bandgap ger låg J_{sc} -ljusström men hög V_{oc} och vice versa. Ofta försöker man med avsikt tillverka solceller med ett högre bandgap vid baksideskontakten än närmare buffertlagret eftersom detta ger ett elektriskt fält som leder de ljusgenererade elektronerna åt rätt håll. Även om det inte gjorts med avsikt så finns det ofta en djupledsvariation i bandgapet hos CIGS-skikten som beror på tillverkningsprocessen.

Karakterisering och modellering av CIGS-solceller

Vi har använt oss av ett antal olika metoder för att mäta egenskaper hos färdiga solceller och enskilda lager Både elektriska och optiska egenskaper

samt materialsammansättningar har studerats. De vanligaste metoderna för att karakterisera färdiga solceller är att mäta ström-spänningsegenskaperna (JV-mätningar) samt att mäta kvantverkningsgraden (QE). Förutom verkningsgraden kan mycket annan information om en solcell fås genom att studera JV-kurvans utseende. QE-mätningar visar hur stor andel av antalet inkommande fotoner som ger upphov till elektron-hålpar som samlas upp i kontakterna. Denna typ av mätning görs som funktion av ljusvåglängd.

De olika materialegenskaper som bestämts har använts som indata till datorsimulering av solcellerna. Resultaten av dessa simuleringar, framförallt JV- och QE-kurvor, jämförs med uppmätta resultat. På detta sätt kan modellen av solcellen utvärderas. Många materialparametrar är relativt okända för våra solceller och kan varieras ganska fritt. De parametrar som vi själva uppmätt eller som är väl kända från litteratur hålls i normalfallet fixa.

Resultat och slutsatser

CIGS-solceller med (Zn,Mg)O-buffertlager får bättre JV-egenskaper när de belyses. Efter en längre tids belysning kommer verkningsgraden, för vissa magnesiumhalter, upp i en nivå högre än hos referensceller med CdS buffert. I mörker sjunker verkningsgraden gradvis under flera veckors tid innan den stabiliseras på en lägre nivå. Mätningar på tunna filmer av (Zn,Mg)O visar att ledningsförmågan för dessa filmer uppvisar ett liknande beteende. Simuleringar visade att egenskaperna hos de färdiga filmerna kunde förklaras med den ökade dopningen i (Zn,Mg)O-lagret. Det verkar även som om det finns en hög koncentration av negativt laddade acceptorer i området runt gränsskiktet mellan CIGS-skiktet och buffertlagret.

Celler med tunna skikt av CuInSe₂ deponerade närmast buffertskiktet studerades med hjälp av datormodellering. Detta modifierade ytlager har inga märkbara vare sig positiva eller negativa effekter på celler med CdS buffertlager. Möjligen skulle ett sådant lager kunna förbättra solceller där rekombination i gränsskiktet är betydande.

Även solceller med olika tjocklek på det ljusabsorberande lagret har undersökts. När CIGS-skikten tunnas ut så ökar först V_{oc} medan J_{sc} minskar. Spänningsökningen beror på mindre rekombination i CIGS-lagret. Strömminskningen å sin sida har sin grund i att mycket ljus nu passerar genom CIGS-skiktet och istället absorberas i bakkontakten. Om absorberskiktet blir tillräckligt tunt så minskar spänningen igen. Detta beror på att koncentrationen av ljusexciterade elektroner blir så hög nära bakkontakten att en omfattande rekombination med hål sker vid denna. För tunna solceller med Zn(O,S) buffert är rekombination vid CIGS/buffert gränsskiktet begränsande för V_{oc} och därmed också för verkningsgraden. Denna typ av rekombination syns inte i tjockare solceller eftersom den då döljs av den dominerande rekombinationen i CIGS-skiktet. Verkningsgraden för normaltjocka celler är på samma nivå

för Zn(O,S)-cellerna och referensceller med CdS. Med tunnare CIGS-skikt är celler med Zn(O,S)-buffert bättre än referenserna. Detta beror på en högre QE-nivå för alla ljusvåglängder över CIGS-bandgapet.

Det som i första hand krävs för att höja verkningsgraden i dessa solceller är att förbättra materialet i CIGS-skiktet. För solcellerna med alternativa buffertlager skulle även gränsskiktet mellan det ljusabsorberande lagret och buffertlagret behöva modifieras för att minska antalet defekter. Nästa steg är att rikta uppmärksamheten mot baksideskontakten och att försöka förbättra dess elektriska egenskaper. Dessa är alla steg på vägen mot att nå en verkningsgrad på över 20.3%, där världsrekordet för CIGS-solceller ligger för tillfället.

Acknowledgements

Many people deserve an acknowledgement for contributing to the work resulting in this thesis. Everyone not named here is thanked as well.

First of all I would like to thank my main supervisor Charlotte. I am deeply grateful that she guided me through my time as a PhD student. I find it hard to imagine a better supervisor. She has consistently shown interest in my work and taken time for discussions. Always full of ideas and with an impressive gift of finding relevant literature. There were never any problems in keeping in touch during her stay as a post-doc in Norway. My visits there were valuable and fun. Thanks for inviting me for dinner in your Norwegian home.

I am also grateful to Marika, my second supervisor. She has been very supportive and open for discussions. Her work in leading the group and retaining financial support is really appreciated.

Thanks to Uwe who always is full of ideas and has helped me out numerous times in the measurement lab. Without him, not much in the lab would be functioning. He is an expert on many things such as electronics, chili, Friday beer and German traditions of flaming punch.

I would like to thank Sebastian for a fruitful collaboration and for being a nice roommate. He is a skilled programmer and always ready to help with computer related issues. His knowledge of Pascal and Matlab has helped me considerably.

It has also been a pleasure sharing rooms with Lina and Per-Oskar. Thanks to Lina for accompanying me for training at times.

With Adam I have had plenty of discussions about the peculiarities of our solar cells, various comedy shows and other fun stuff. Thanks to him and Tobias for providing great ALD thin films and buffer layers. Tobias has also provided some great lunch laughs in his own pessimistic way. The only rival to him when it comes to gallows humour must be Jens. Good luck to him now that his destination, a dissertation, finally approaches.

Piotr did a great work upgrading the IVT-setup with capacitance and LED facilities. May the force be with him in his endeavour towards a PhD.

Thanks to my other fellow PhD students in the group; Timo, Tove and Johan as well as the post-docs; Pedro and Jonathan and our engineer Viktor for being such nice colleagues. Viktor has had to suffer many pains with the disobedient QE-setup, now when I have been busy writing thesis. I also send my regards to former members of the group. I would like to mention Ulf who helped introducing me to the equipment in the measurement lab.

The Solibro crew has been good company in the measurement lab.

I would also like to thank the rest of my colleagues in the division. Some special thanks to our secretary Marianne who has given invaluable help on everything administrative.

Arve Holt is acknowledged for letting me come and work in the solar cell group at IFE in Lilleström. He and all his colleagues made the stay there very enjoyable. Thanks also to Anna for helping me to sort out things when a few annoying incidents had happened in Norway.

The Nordic Centre of Excellence in Photovoltaics and the Swedish Energy Agency are acknowledged for their financial support.

Finally, a warm thanks to all of my friends, to my parents and to the rest of the family for their support.

Bibliography

- [1] ‘Directive 2002/95/EC’. URL <http://eur-lex.europa.eu>.
- [2] D. Abou-Ras, R. Caballero, C.-H. Fischer, C.A. Kaufmann, I. Lauermann, R. Mainz, H. Mönig, A. Schöpke, C. Stephan, C. Streeck, S. Schorr, A. Eicke, M. Döbeli, B. Gade, J. Hinrichs, T. Nunney, H. Dijkstra, V. Hoffmann, D. Klemm, V. Efimova, A. Bergmaier, G. Dollinger, T. Wirth, W. Unger, A.A. Rockett, A. Perez-Rodriguez, J. Alvarez-Garcia, V. Izquierdo-Roca, T. Schmid, P.-P. Choi, M. Müller, F. Bertram, J. Christen, H. Khatri, R.W. Collins, S. Marsillac, and I. Kötschau (2011). ‘Comprehensive Comparison of Various Techniques for the Analysis of Elemental Distributions in Thin Films’. *Microscopy and Microanalysis* **17** (05), pp. 728–751. doi:10.1017/S1431927611000523.
- [3] Daniel Abou-Ras, Debashis Mukherji, Gernot Kostorz, David Brémaud, Marc Kälin, Dominik Rudmann, Max Döbeli, and Ayodhya N. Tiwari (2005). ‘Dependence of the MoSe₂ Formation on the Mo Orientation and the Na Concentration for Cu(In,Ga)Se₂ Thin-Film Solar Cells’. *MRS Online Proceedings Library* **865**. doi:10.1557/PROC-865-F8.1.
- [4] María Isabel Alonso, Miquel Garriga, Carlos Alberto Durante Rincón, Elvis Hernández, and Máximo León (2002). ‘Optical functions of chalcopyrite CuGa_xIn_{1-x}Se₂ alloys’. *Applied Physics A: Materials Science & Processing* **74**, pp. 659–664. doi:10.1007/s003390100931.
- [5] L. Assmann, J.C. Bernède, A. Drici, C. Amory, E. Halgand, and M. Morsli (2005). ‘Study of the Mo thin films and Mo/CIGS interface properties’. *Applied Surface Science* **246** (1-3), pp. 159 – 166. doi:10.1016/j.apsusc.2004.11.020.
- [6] Various Authors (2011). ‘Key World Energy Statistics’. Tech. rep., International Energy Agency. URL http://www.iea.org/textbase/nppdf/free/2011/key_world_energy_stats.pdf.
- [7] M. Bodegård, J. Kessler, O. Lundberg, J. Schöldström, and L. Stolt, ‘Growth of Co-evaporated Cu(In,Ga)Se₂ - The Influence of Rate Profiles on Film Morphology’. In ‘MRS Proceedings’, vol. 668, p. H2.2 (2001). doi:10.1557/PROC-668-H2.2.
- [8] Marc Burgelman and Jonas Marlein, ‘Analysis of graded band gap solar cells with SCAPS’. In ‘Proceedings of the 23rd European Photovoltaic Solar Energy Conference’, p. 2151 (2008).
- [9] Marc Burgelman, Peter Nollet, and Stefaan Degraeve (2000). ‘Modelling polycrystalline semiconductor solar cells’. *Thin Solid Films* **361–362**, pp. 527–532. doi:10.1016/S0040-6090(99)00825-1.

- [10] R. Caballero, C.A. Kaufmann, T. Eisenbarth, A. Grimm, I. Lauermann, T. Unold, R. Klenk, and H.W. Schock (2010). 'Influence of Na on Cu(In,Ga)Se₂ solar cells grown on polyimide substrates at low temperature: Impact on the Cu(In,Ga)Se₂/Mo interface'. *Applied Physics Letters* **96** (9), p. 092104. doi:10.1063/1.3340459.
- [11] B. Claflin, D.C. Look, S.J. Park, and G. Cantwell (2006). 'Persistent n-type photoconductivity in p-type ZnO'. *Journal of Crystal Growth* **287** (1), pp. 16 – 22. doi:10.1016/j.jcrysgro.2005.10.035.
- [12] D A Clugston and P A Basore, 'PC1D version 5: 32-bit solar cell modeling on personal computers'. In 'Conference Record of the Twenty Sixth IEEE Photovoltaic Specialists Conference 1997', October, pp. 207–210 (1997). doi: 10.1109/PVSC.1997.654065.
- [13] A. S. Dissanayake, S. X. Huang, H. X. Jiang, and J. Y. Lin (1991). 'Charge storage and persistent photoconductivity in a CdS_{0.5}Se_{0.5} semiconductor alloy'. *Phys. Rev. B* **44**, pp. 13343–13348. doi:10.1103/PhysRevB.44.13343.
- [14] A. S. Dissanayake, J. Y. Lin, and H. X. Jiang (1993). 'Persistent photoconductivity in Zn_{0.04}Cd_{0.96}Te semiconductor thin films'. *Phys. Rev. B* **48**, pp. 8145–8151. doi:10.1103/PhysRevB.48.8145.
- [15] M. Edoff, S Woldegiorgis, P Neretnieks, M Ruth, J Kessler, and L Stolt, 'CIGS submodules with high performance and high manufacturability'. In 'Proceedings of the 19th European Photovoltaic Solar Energy Conference', pp. 1690–193 (Paris, France, 2004).
- [16] Stephen J. Fonash, *Solar Cell Device Physics* (Academic Press Inc., New York, USA, 1981), 1 ed.
- [17] A. Froitzheim, R. Stangl, L. Elstner, M. Kriegel, and W. Fuhs, 'AFORS-HET: a computer-program for the simulation of heterojunction solar cells to be distributed for public use'. In 'Photovoltaic Energy Conversion, 2003. Proceedings of 3rd World Conference on', vol. 1, pp. 279 –282 Vol.1 (2003). URL http://ieeexplore.ieee.org/xpls/abs_all.jsp?arnumber=1305276&tag=1.
- [18] Andrew M. Gabor, John R. Tuttle, David S. Albin, Miguel A. Contreras, Rommel Noufi, and Allen M. Hermann (1994). 'High-efficiency CuIn_xGa_{1-x}Se₂ solar cells made from (In_xGa_{1-x})₂Se₃ precursor films'. *Applied Physics Letters* **65** (2), pp. 198–200. doi:10.1063/1.112670.
- [19] M. Gloeckler, A.L. Fahrenbruch, and J.R. Sites, 'Numerical modeling of CIGS and CdTe solar cells: setting the baseline'. In 'Photovoltaic Energy Conversion, 2003. Proceedings of 3rd World Conference on', vol. 1, pp. 491 –494 Vol.1 (2003).
- [20] Hubert Gnaser (1994). 'Improved quantification in secondary-ion mass spectrometry detecting MCs⁺ molecular ions'. *Journal of Vacuum Science & Technology A: Vacuum, Surfaces, and Films* **12** (2), pp. 452–456. doi:10.1116/1.579262.

- [21] Martin A. Green, Keith Emery, Yoshihiro Hishikawa, Wilhelm Warta, and Ewan D. Dunlop (2011). ‘Solar cell efficiency tables (Version 38)’. *Progress in Photovoltaics: Research and Applications* **19** (5), pp. 565–572. doi:10.1002/pip.1150.
- [22] Jennifer Heath and Pawel Zabierowski, *Capacitance Spectroscopy of Thin-Film Solar Cells*, pp. 81–105 (Wiley-VCH Verlag GmbH & Co. KGaA, 2011). ISBN 9783527636280. doi:10.1002/9783527636280.ch4.
- [23] JT Heath, JD Cohen, and WN Shafarman (2003). ‘Distinguishing metastable changes in bulk CIGS defect densities from interface effects’. *THIN SOLID FILMS* **431**, pp. 426–430. doi:10.1016/S0040-6090(03)00189-5. Spring Meeting of the European-Materials-Research-Society (E-MRS), STRASBOURG, FRANCE, JUN 18-21, 2002.
- [24] Steven Hegedus and William N. Shafarman (2004). ‘Thin-film solar cells: Device measurements and analysis’. *Progress in Photovoltaics: Research and Applications* **12** (2–3), pp. 155–176. doi:10.1002/pip.518.
- [25] Philip Jackson, Dimitrios Hariskos, Erwin Lotter, Stefan Paetel, Roland Wuerz, Richard Menner, Wiltraud Wischmann, and Michael Powalla (2011). ‘New world record efficiency for Cu(In,Ga)Se₂ thin-film solar cells beyond 20%’. *Progress in Photovoltaics: Research and Applications* **19** (7), pp. 894–897. doi:10.1002/pip.1078.
- [26] Philip Jackson, Roland Wurz, Uwe Rau, Julian Mattheis, Matthias Kurth, Thomas Schlötzer, Gerhard Bilger, and Jürgen H. Werner (2007). ‘High-quality baseline for high efficiency CuIn_{1-x}Ga_xSe₂ solar cells’. *Progress in Photovoltaics: Research and Applications* **15** (6), pp. 507–19. doi:10.1002/pip.757.
- [27] H. X. Jiang, G. Brown, and J. Y. Lin (1991). ‘Persistent photoconductivity in II-VI and III-V semiconductor alloys and a novel infrared detector’. *Journal of Applied Physics* **69** (9), pp. 6701–6703. doi:10.1063/1.348889.
- [28] H. X. Jiang, A. Dissanayake, and J. Y. Lin (1992). ‘Band-tail states in a Zn_{0.3}Cd_{0.7}Se semiconductor alloy probed by persistent photoconductivity’. *Phys. Rev. B* **45**, pp. 4520–4523. doi:10.1103/PhysRevB.45.4520.
- [29] Marianna Kemell, Mikko Ritala, and Markku Leskelä (2005). ‘Thin Film Deposition Methods for CuInSe₂ Solar Cells’. *Critical Reviews in Solid State and Materials Sciences* **30** (1), pp. 1–31. doi:10.1080/10408430590918341.
- [30] John Kessler, Marika Bodegård, Jonas Hedström, and Lars Stolt (2001). ‘Baseline Cu(In,Ga)Se₂ device production: control and statistical significance’. *Solar Energy Materials and Solar Cells* **67** (1–4), pp. 67–76. doi:10.1016/S0927-0248(00)00264-6.
- [31] A Klein and T Schulmeyer, ‘Interfaces of Cu-Chalcopyrites’. In Susanne Siebentritt and Uwe Rau (editors), ‘Wide-Gap Chalcopyrites’, vol. 86 of *Springer Series in Materials Science*, pp. 213–233 (Springer Berlin Heidelberg, 2006). ISBN 978-3-540-31293-2. doi:10.1007/3-540-31293-5_11.

- [32] Naoki Kohara, Shiro Nishiwaki, Yasuhiro Hashimoto, Takayuki Negami, and Takahiro Wada (2001). ‘Electrical properties of the Cu(In,Ga)Se₂/MoSe₂/Mo structure’. *Solar Energy Materials and Solar Cells* **67** (1-4), pp. 209–215. doi: 10.1016/S0927-0248(00)00283-X.
- [33] Immo M. Kötschau and Hans-Werner Schock (2003). ‘Depth profile of the lattice constant of the Cu-poor surface layer in (Cu₂Se)_{1-x}(In₂Se₃)_x evidenced by grazing incidence X-ray diffraction’. *Journal of Physics and Chemistry of Solids* **64** (9–10), pp. 1559–1563. doi:10.1016/S0022-3697(03)00074-X. Proceedings of the 13th International Conference on Ternary and Multinary Compounds.
- [34] D. V. Lang and R. A. Logan (1977). ‘Large-Lattice-Relaxation Model for Persistent Photoconductivity in Compound Semiconductors’. *Phys. Rev. Lett.* **39**, pp. 635–639. doi:10.1103/PhysRevLett.39.635.
- [35] D. V. Lang, R. A. Logan, and M. Jaros (1979). ‘Trapping characteristics and a donor-complex (DX) model for the persistent-photoconductivity trapping center in Te-doped Al_xGa_{1-x}As’. *Phys. Rev. B* **19**, pp. 1015–1030. doi: 10.1103/PhysRevB.19.1015.
- [36] Stephan Lany and Alex Zunger (2005). ‘Anion vacancies as a source of persistent photoconductivity in II-VI and chalcopyrite semiconductors’. *Phys. Rev. B* **72**, p. 035215. doi:10.1103/PhysRevB.72.035215.
- [37] Stephan Lany and Alex Zunger (2006). ‘Light- and bias-induced metastabilities in Cu(In,Ga)Se₂ based solar cells caused by the (VSe-VCu) vacancy complex’. *Journal of Applied Physics* **100** (11), 113725. doi:10.1063/1.2388256.
- [38] Dongxiang Liao and Angus Rockett (2003). ‘Cu depletion at the CuInSe₂ surface’. *Applied Physics Letters* **82** (17), pp. 2829–2831. doi:10.1063/1.1570516.
- [39] T. Loher, W. Jaegermann, and C. Pettenkofer (1995). ‘Formation and electronic properties of the CdS/CuInSe₂ (011) heterointerface studied by synchrotron-induced photoemission’. *Journal of Applied Physics* **77** (2), pp. 731–738. doi: 10.1063/1.359583.
- [40] Ulf Malm, Jonas Malmström, Charlotte Platzer-Björkman, and Lars Stolt (2005). ‘Determination of dominant recombination paths in Cu(In,Ga)Se₂ thin-film solar cells with ALD-ZnO buffer layers’. *Thin Solid Films* **480–481**, pp. 208–12. doi:10.1016/j.tsf.2004.11.008.
- [41] Jonas Malmström (2005). *On Generation and Recombination in Cu(In,Ga)Se₂ Thin-Film Solar Cells*. Ph.D. thesis, Uppsala University, Solid State Electronics. URL <http://urn.kb.se/resolve?urn=urn:nbn:se:uu:diva-5721>.
- [42] Wyatt K. Metzger (2008). ‘The potential and device physics of interdigitated thin-film solar cells’. *Journal of Applied Physics* **103** (9), p. 094515. doi:10.1063/1.2913502.

- [43] M. Morkel, L. Weinhardt, B. Lohmuller, C. Heske, E. Umbach, W. Riedl, S. Zweigart, and F. Karg (2001). 'Flat conduction-band alignment at the CdS/CuInSe₂ thin-film solar-cell heterojunction'. *Applied Physics Letters* **79** (27), pp. 4482–4484. doi:10.1063/1.1428408.
- [44] Shiro Nishiwaki, Naoki Kohara, Takayuki Negami, and Takahiro Wada (1998). 'MoSe₂ layer formation at Cu(In,Ga)Se₂/Mo Interfaces in High Efficiency CuIn_{1-x}Ga_xSe₂ Solar Cells'. *Japanese Journal of Applied Physics* **37** (Part 2, No. 1A/B), pp. L71–L73. doi:10.1143/JJAP.37.L71.
- [45] The National Institute of Standards and Technology (NIST). 'Hall effect measurements'. URL <http://www.nist.gov/pml/div683/hall.cfm>.
- [46] J W Orton and M J Powell (1980). 'The Hall effect in polycrystalline and powdered semiconductors'. *Reports on Progress in Physics* **43** (11), p. 1263. doi:10.1088/0034-4885/43/11/001.
- [47] C. Platzer-Bjorkman, T. Torndahl, D. Abou-Ras, J. Malmstrom, J. Kessler, and L. Stolt (2006). 'Zn(O,S) buffer layers by atomic layer deposition in Cu(In,Ga)Se₂ based thin film solar cells: Band alignment and sulfur gradient'. *Journal of Applied Physics* **100** (4), 044506. doi:10.1063/1.2222067.
- [48] Charlotte Platzer-Björkman (2006). *Band Alignment Between ZnO-Based and Cu(In,Ga)Se₂ Thin Films for High Efficiency Solar Cells*. Ph.D. thesis, Uppsala University, Solid State Electronics. URL <http://urn.kb.se/resolve?urn=urn:nbn:se:uu:diva-6263>.
- [49] Charlotte Platzer-Björkman, John Kessler, and Lars Stolt, 'Atomic layer deposition of Zn(O,S) buffer layers for high efficiency Cu(In,Ga)Se₂ solar cells'. In 'Proceedings of the 3rd World Conference on Photovoltaic Energy Conversion', pp. 461–464 (Osaka, 2003).
- [50] Charlotte Platzer-Björkman, J. Lu, John Kessler, and Lars Stolt (2003). 'Interface study of CuInSe₂/ZnO and Cu(In,Ga)Se₂/ZnO devices using ALD ZnO buffer layers'. *Thin Solid Films* **431–432**, pp. 321–5. doi:10.1016/s0040-6090(03)00229-3.
- [51] A. Polyakov, N. Smirnov, A. Govorkov, E. Kozhukhova, S. Pearton, D. Norton, A. Osinsky, and Amir Dabiran (2006). 'Electrical properties of undoped bulk ZnO substrates'. *Journal of Electronic Materials* **35**, pp. 663–669. doi:10.1007/s11664-006-0117-x. 10.1007/s11664-006-0117-x.
- [52] A. Y. Polyakov, N. B. Smirnov, A. V. Govorkov, A. I. Belogorokhov, E. A. Kozhukhova, A. V. Markov, A. Osinsky, J. W. Dong, and S. J. Pearton (2007). 'Persistent photoconductivity in p-type ZnO(N) grown by molecular beam epitaxy'. *Applied Physics Letters* **90** (13), 132103. doi:10.1063/1.2717089.
- [53] A. Y. Polyakov, N. B. Smirnov, A. V. Govorkov, E. A. Kozhukhova, A. I. Belogorokhov, A. V. Markov, H. S. Kim, D. P. Norton, and S. J. Pearton (2007). 'Electrical Properties of ZnO(P) and ZnMgO(P) Films Grown by Pulsed Laser

- Deposition'. *Journal of The Electrochemical Society* **154** (9), pp. H825–H829. doi:10.1149/1.2756976.
- [54] E. H. Putley, *The Hall Effect and Related Phenomena* (Butterworths, London, 1960).
- [55] H. J. Queisser and D. E. Theodorou (1986). 'Decay kinetics of persistent photoconductivity in semiconductors'. *Phys. Rev. B* **33**, pp. 4027–4033. doi:10.1103/PhysRevB.33.4027.
- [56] U Rau, A Jasenek, H.W Schock, F Engelhardt, and Th Meyer (2000). 'Electronic loss mechanisms in chalcopyrite based heterojunction solar cells'. *Thin Solid Films* **361-362** (0), pp. 298 – 302. doi:10.1016/S0040-6090(99)00762-2.
- [57] U. Rau, M. Schmitt, J. Parisi, W. Riedl, and F. Karg (1998). 'Persistent photoconductivity in Cu(In,Ga)Se₂ heterojunctions and thin films prepared by sequential deposition'. *Applied Physics Letters* **73** (2), pp. 223–225. doi:10.1063/1.121762.
- [58] Uwe Rau and Hans-Werner Schock, 'Cu(In,Ga)Se₂ solar cells'. In Mary D. Archer and Robert Hill (editors), 'Clean Energy from Photovoltaics', chap. 7, pp. 277–345 (Imperial College Press, 2001). ISBN 978-1-60119-771-9.
- [59] Ingrid L. Repins, Miguel A. Contreras, Brian Egaas, Clay DeHart, John Scharf, Craig L. Perkins, Bobby To, and Rommel Noufi (2008). '19.9 %-efficient ZnO/CdS/CuInGaSe₂ Solar Cell with 81.2 % Fill Factor'. *Progress in Photovoltaics: Research and Applications* **16**, pp. 235–239. doi:10.1002/pip.822.
- [60] M.N. Ruberto and A. Rothwarf, 'An experimental and theoretical study of the time dependent open circuit voltage in CuInSe₂/CdS solar cells'. In 'Conference Record of the Nineteenth IEEE Photovoltaic Specialists Conference - 1987 (Cat. No.87CH2400-0)', pp. 1329–34. IEEE (IEEE, New York, NY, USA, 1987). Conference Record of the Nineteenth IEEE Photovoltaic Specialists Conference - 1987 (Cat. No.87CH2400-0), 4-8 May 1987, New Orleans, LA, USA.
- [61] Roland Scheer (2009). 'Activation energy of heterojunction diode currents in the limit of interface recombination'. *Journal of Applied Physics* **105** (10), p. 104505. doi:DOI:10.1063/1.3126523.
- [62] Sebastian Michael Schleussner (2011). *ZrN Back-Contact Reflectors and Ga Gradients in Cu(In,Ga)Se₂ Solar Cells*. Ph.D. thesis, Uppsala University, Solid State Electronics. URL <http://urn.kb.se/resolve?urn=urn:nbn:se:uu:diva-151402>. 70 pages.
- [63] Dieter Schmid, Martin Ruckh, F. Grunwald, and Hans-Werner Schock (1993). 'Chalcopyrite/defect chalcopyrite heterojunctions on the basis of CuInSe₂'. *Journal of Applied Physics* **73**, pp. 2902–2909. doi:10.1063/1.353020.
- [64] Dieter Schmid, Martin Ruckh, and Hans Werner Schock (1996). 'A comprehensive characterization of the interfaces in Mo/CIS/CdS/ZnO solar cell structures'. *Solar Energy Materials and Solar Cells* **41-42** (0), pp. 281–294. doi:10.1016/0927-0248(95)00107-7.

- [65] Dieter Schmid, Martin Ruckh, and Hans-Werner Schock (1996). 'Photoemission studies on Cu(In,Ga)Se₂ thin films and related binary selenides'. *Applied Surface Science* **103** (4), pp. 409–429. doi:10.1016/S0169-4332(96)00099-2.
- [66] Dieter K. Schroder, *Semiconductor material and device characterization* (John Wiley & Sons Inc., Hoboken, New Jersey, 2006), 3 ed.
- [67] William N. Shafarman and Lars Stolt, 'Cu(In,Ga)Se₂ Solar Cells'. In Antonio Luque and Steven Hegedus (editors), 'Handbook of Photovoltaic Science and Engineering', chap. 13, pp. 567–616 (John Wiley & Sons Inc., 2003). ISBN 0-471-49196-9. URL <http://www.knovel.com/web/portal/browse/>.
- [68] Shik A. A. Sheinkman M. K. (1976). 'Long-term relaxation and residual conductivity of semiconductors'. *Soviet Physics-Semiconductors* **10** (2), pp. 128–143.
- [69] SILVACO. 'ATLAS - Device Simulation Framework'. URL http://www.silvaco.com/products/device_simulation/atlas.html.
- [70] R. A. Smith, *Semiconductors* (Cambridge university press, Cambridge, Great Britain, 1978), 2 ed.
- [71] S. M. Sze and Kwok K. Ng, *Physics of Semiconductor Devices* (John Wiley & Sons Inc., Hoboken, New Jersey, 2007), 3 ed.
- [72] T. Törndahl, C. Platzer-Björkman, J. Kessler, and M. Edoff (2007). 'Atomic layer deposition of Zn_{1-x}Mg_xO buffer layers for Cu(In,Ga)Se₂ solar cells'. *Progress in Photovoltaics: Research and Applications* **15** (3), pp. 225–235. doi:10.1002/pip.733.
- [73] J. Verschraegen and M. Burgelman (2007). 'Numerical modeling of intra-band tunneling for heterojunction solar cells in scaps'. *Thin Solid Films* **515** (15), pp. 6276 – 6279. doi:10.1016/j.tsf.2006.12.049.
- [74] R. Würz, D. Fuertes Marrón, A. Meeder, A. Rumberg, S.M. Babu, Th. Schedel-Niedrig, U. Bloeck, P. Schubert-Bischoff, and M.Ch. Lux-Steiner (2003). 'Formation of an interfacial MoSe₂ layer in CVD grown CuGaSe₂ based thin film solar cells'. *Thin Solid Films* **431-432** (0), pp. 398 – 402. doi:10.1016/S0040-6090(03)00261-X.
- [75] P. Zabierowski and C. Platzer-Björkman, 'Influence of metastabilities on the efficiency of CIGSe-based solar cells with CdS, Zn(O,S) and (Zn,Mg)O buffers'. In 'Proceedings of the 22nd European Photovoltaic Solar Energy Conference', pp. 2395–2400 (Milano, 2007).
- [76] Pawel Zabierowski, *Thin Film Solar Cells: Current Status and Future Trends*, chap. Electrical characterization of Cu(In,Ga)Se₂ - based thin film photovoltaic devices, pp. 1–31 (Nova Science Publishers, Inc., 2011).

- [77] S. B. Zhang, Su-Huai Wei, Alex Zunger, and H. Katayama-Yoshida (1998). ‘Defect physics of the CuInSe₂ chalcopyrite semiconductor’. *Phys. Rev. B* **57**, pp. 9642–9656. doi:10.1103/PhysRevB.57.9642.

Acta Universitatis Upsaliensis

*Digital Comprehensive Summaries of Uppsala Dissertations
from the Faculty of Science and Technology 900*

Editor: The Dean of the Faculty of Science and Technology

A doctoral dissertation from the Faculty of Science and Technology, Uppsala University, is usually a summary of a number of papers. A few copies of the complete dissertation are kept at major Swedish research libraries, while the summary alone is distributed internationally through the series Digital Comprehensive Summaries of Uppsala Dissertations from the Faculty of Science and Technology.



ACTA
UNIVERSITATIS
UPSALIENSIS
UPPSALA
2012

Distribution: publications.uu.se
urn:nbn:se:uu:diva-168618